

KINEMATICS AND CHEMISTRY OF STARS ALONG THE SAGITTARIUS TRAILING TIDAL TAIL AND CONSTRAINTS ON THE MILKY WAY MASS DISTRIBUTION

JEFFREY L. CARLIN^{1,2,5}, STEVEN R. MAJEWSKI¹, DANA I. CASETTI-DINESCU³, DAVID R. LAW⁴, TERRENCE M. GIRARD³, AND RICHARD J. PATTERSON¹

Draft version August 29, 2018

ABSTRACT

We present three-dimensional kinematics of Sagittarius (Sgr) trailing tidal debris in six fields located 70–130° along the stream from the Sgr dwarf galaxy core. The data are from our proper-motion (PM) survey of Kapteyn’s Selected Areas, in which we have measured accurate PMs to faint magnitudes in $\sim 40' \times 40'$ fields evenly spaced across the sky. The radial velocity (RV) signature of Sgr has been identified among our follow-up spectroscopic data in four of the six fields and combined with mean PMs of spectroscopically-confirmed members to derive space motions of Sgr debris based on ~ 15 –64 confirmed stream members per field. These kinematics are compared to predictions of the Law & Majewski (2010a) model of Sgr disruption; we find reasonable agreement with model predictions in RVs and PMs along Galactic latitude. However, an upward adjustment of the Local Standard of Rest velocity (Θ_{LSR}) from its standard 220 km s^{−1} to at least 232 ± 14 km s^{−1} (and possibly as high as 264 ± 23 km s^{−1}) is necessary to bring 3-D model debris kinematics and our measurements into agreement. Satisfactory model fits that simultaneously reproduce known position, distance, and radial velocity trends of the Sgr tidal streams, while significantly increasing Θ_{LSR} , could only be achieved by increasing the Galactic bulge and disk mass while leaving the dark matter halo fixed to the best-fit values from Law & Majewski (2010a). We derive low-resolution spectroscopic abundances along this stretch of the Sgr stream and find a constant $[\text{Fe}/\text{H}] \sim -1.15$ (with ~ 0.5 dex scatter in each field – typical for dwarf galaxy populations) among the four fields with reliable measurements. A constant metallicity suggests that debris along the $\sim 60^\circ$ span of this study was all stripped from Sgr on the same orbital passage.

Subject headings: Galaxies: individual: (Sagittarius dwarf spheroidal) — Galaxy: fundamental parameters — Galaxy: kinematics and dynamics — Galaxy: structure

1. INTRODUCTION

With the profusion of data provided in recent years by deep, large-area photometric surveys such as the Two Micron All Sky Survey (2MASS) and Sloan Digital Sky Survey (SDSS), a wealth of stellar substructure has been uncovered in the Milky Way (MW) halo. The finding and subsequent mapping of numerous stellar tidal streams and overdensities (e.g., Sagittarius — Ibata et al. 2001; Majewski et al. 2003; Belokurov et al. 2006; Monoceros — Newberg et al. 2002; Ibata et al. 2003; Yanny et al. 2003; other SDSS streams — Grillmair 2009; Belokurov et al. 2007; Grillmair 2006a,b; Grillmair & Dionatos 2006) has borne out the idea (Searle & Zinn 1978; Majewski 1993; Majewski et al. 1996) that remnants of accreted dwarf galaxies make up much of the stellar halo of the Milky Way. The direct confirmation of the accretion of late-infalling subhalos via discovery of ubiquitous long-lived, coherent tidal debris streams has provided strong constraints on models of small-scale hierarchical structure formation under the prevailing Λ -Cold

Dark Matter (Λ CDM) cosmology (e.g., Abadi et al. 2003; Bullock & Johnston 2005; Font et al. 2006). Furthermore, because the tidal streams retain the kinematical signatures of the orbits of their progenitors (i.e., angular momentum and energy), stellar debris in the streams can be used as sensitive probes of the underlying Galactic gravitational potential (e.g., Johnston et al. 1999; Ibata et al. 2001; Helmi 2004; Martínez-Delgado et al. 2004; Johnston et al. 2005; Law et al. 2005; Majewski et al. 2006).

The best-known and *only* widely agreed-upon case of a presently visible dwarf galaxy undergoing tidal disruption in the Milky Way halo is the Sagittarius (Sgr) dwarf spheroidal (dSph)⁶. The core of this galaxy was first discovered by Ibata et al. (1994) in a kinematical study of the outer Galactic bulge, with the first large-scale mapping of the Sgr leading and trailing tidal arms done by Majewski et al. (2003) using 2MASS M-giant stars. Various studies have reported the discovery of stars (e.g., Majewski et al. 2003; Martínez-Delgado et al. 2004; Belokurov et al. 2006; Yanny et al. 2009b; Correnti et al. 2010; a comprehensive summary of the earlier detections appears in Majewski et al. 2003) or star clusters (e.g., Pal 12: Dinescu et al. 2000; Whiting 1: Carraro et al. 2007; many clusters: Bellazzini et al. 2003; a summary of Sgr clusters appears in Law & Majewski 2010b) plausibly associated with debris from Sgr, either trailing or leading it along its orbit. Line-of-sight ve-

¹ Department of Astronomy, University of Virginia, P.O. Box 400325, Charlottesville, VA 22904-4325, USA (jc4qn@mail.astro.virginia.edu)

² Department of Physics, Applied Physics, and Astronomy, Rensselaer Polytechnic Institute, 110 8th Street, Troy, NY 12180, USA (carlij@rpi.edu)

³ Astronomy Department, Yale University, P.O. Box 208101, New Haven, CT 06520-8101, USA

⁴ Department of Physics and Astronomy, University of California, Los Angeles, CA 90095, USA ; Hubble Fellow

⁵ Visiting Astronomer, Kitt Peak National Observatory, National Optical Astronomy Observatory, which is operated by the Association of Universities for Research in Astronomy (AURA) under cooperative agreement with the National Science Foundation.

⁶ Though we note that there is now evidence for extended tidal debris populations around the Carina (Muñoz et al. 2006b, 2008) and Leo I (Sohn et al. 2007) dSphs. Also, some debate still exists over whether the HI Magellanic Stream derives from tidal stripping of Small or Large Magellanic Cloud gas versus from ram pressure stripping.

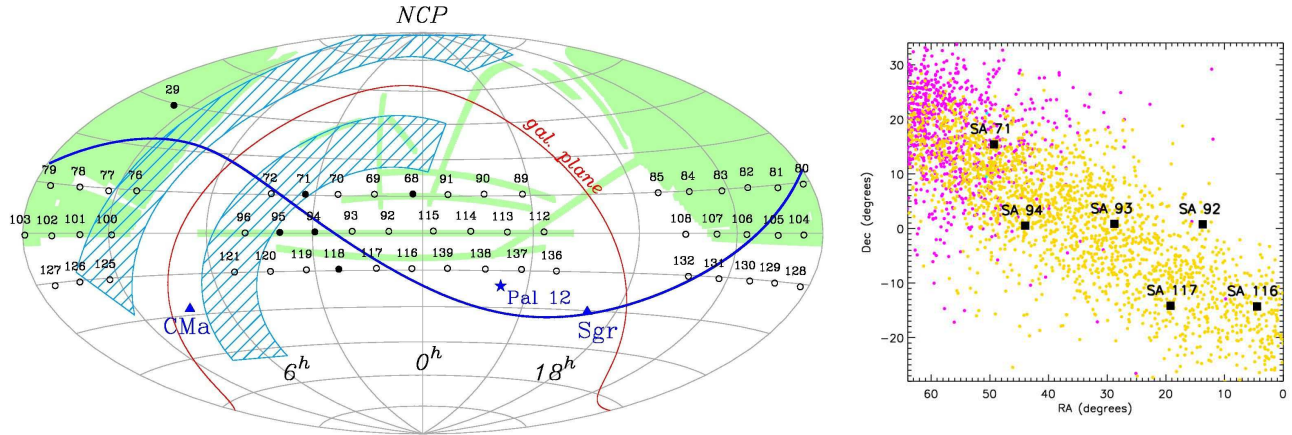


Figure 1. *Left panel:* Distribution of Kapteyn's Selected Areas (in equatorial coordinates) for which we have derived proper motions, shown in an Aitoff projection. Solid points are those fields for which we have additional deep, 4-meter plates (see text). The current orbital plane of Sagittarius is overlaid as a solid blue line, and the shaded (light green) areas represent the sky coverage of SDSS (as of DR5). Regions containing stellar overdensities suggested in the literature to be part of the "Monoceros ring" are denoted by the blue hatched areas on either side of the disk. *Right panel:* Spatial distribution of the Kapteyn Selected Areas used in this study overlaid on the predicted distribution of Sagittarius tidal debris from the best-fit triaxial halo model of Law & Majewski (2010a). Gold colored points represent debris stripped from the Sgr progenitor on the past two perigalactic passages (0-1.3 Gyr ago), and magenta points the previous two passages (1.3-3.2 Gyr ago). Note that all of the fields are sampling predominantly debris stripped on the same orbital passage (i.e., the gold points), with only SA 71 slightly sampling earlier-stripped (magenta) debris.

locities (i.e., *radial velocities*, or RVs) of Sgr members have been determined at a few positions along the stream (e.g., Dohm-Palmer et al. 2001; Majewski et al. 2004; Monaco et al. 2007), and, along with the spatial distribution of these stars, provide constraints on models of the Sgr-Milky Way interaction (e.g., Johnston et al. 1995; Helmi & White 2001; Ibata et al. 2001; Helmi 2004; Martínez-Delgado et al. 2004). A comprehensive effort at modeling the Sgr disruption constrained by all observations available after about a decade of study was done by Law et al. (2005), who were able to reproduce most extant data, but were unable to completely reconcile the apparent need for a prolate MW halo potential to produce the leading arm *radial velocities* on the one hand, and an oblate halo to match the *positions* of leading debris on the other. This contradiction has apparently been recently resolved by Law et al. (2009), who propose that the Milky Way might have a triaxial halo; a comprehensive *N*-body model based on the best-fitting triaxial halo (Law & Majewski 2010a, hereafter LM10) reasonably matches nearly all existing constraints (spatial and kinematical) of Sgr tidal debris.⁷ The Sagittarius dwarf and its tidal debris are thus proving to be an excellent laboratory for studying both the dynamics of tidally disrupting dwarf galaxies and star stream formation, as well as the shape and strength of the Galactic gravitational potential that is the cause of this disruption. It is this model of LM10 to which we shall compare our data throughout this work.

1.1. Our Proper Motion Survey

⁷ Further complications have arisen due to an apparent bifurcation of the leading stream (Belokurov et al. 2006); the LM10 model was not designed to address this issue. Several attempts to explain this detail invoke overlapping debris from multiple orbital wraps (Fellhauer et al. 2006; though Yanny et al. 2009b find similar stellar populations in both arms, likely ruling out this scenario) or a disk-galaxy progenitor for Sgr (Peñarrubia et al. 2010; but cf. Łokas et al. 2010). The highly-elliptical shape of the Sgr dwarf has recently been reproduced by (Łokas et al. 2010), who model Sgr as a disk galaxy embedded in an extended dark halo. Tidal stirring transforms the initially disk dwarf into an extended elliptical shape over two pericentric passages; the rotation of the progenitor may also explain the bifurcation of the Sgr leading arm.

To date, no systematic survey has addressed the tangential velocities (derived from proper motions) of the identified major Galactic tidal streams. Only a few studies (e.g., Dinescu et al. 2002; Casetti-Dinescu et al. 2008, 2009; Carlin et al. 2010; Koposov et al. 2010) have published *any* proper motion results for major Galactic substructures, and typically not at a level of precision that is useful for constraining dynamical models of tidal stream production and evolution. In an effort to detect and characterize halo substructures, we have been working on a project to obtain full phase-space information (positions and full 3-D space motions) for individual stars in Kapteyn's Selected Areas (SAs; see Casetti-Dinescu et al. 2006 for an overview of this project). The sky positions of the Selected Areas were chosen by Jacobus Kapteyn (1906) to provide evenly spaced coverage for a systematic exploration of Milky Way structure. We have attempted to carry on at least part of this legacy by taking advantage of Mt. Wilson 60-inch telescope photographic plate material taken by Kapteyn and collaborators (Seares et al. 1930) for their survey to make up the first-epoch data of our survey (in particular, near-equatorial fields at $\delta = 0^\circ$, $+15^\circ$, and -15°). The distribution on the sky of those SAs that make up our survey is shown in an Aitoff projection in Figure 1. Some of the equatorial SA fields lie along the orbit of the Sagittarius dwarf galaxy (which is approximated by the blue, solid curve in Figure 1) – it is a subset of these fields (in particular, six fields along the trailing tidal tail; see the right panel of Figure 1) that are the focus of the present work.

1.2. Constraints on the Local Standard of Rest Velocity

The positions of tidal debris that have been found over a large stretch of the Sagittarius orbit place fairly strong constraints on the three-dimensional motions of the Sgr dwarf. It is, however, important to confirm and refine the models by measuring space velocities of stream stars (especially proper motions, which are difficult to measure for stars in distant Galactic substructures). In the case of the Sgr trailing tail, however, proper motions measured for debris stars are also rather sensitive to the Sun's motion through the Galaxy. This arises because much of the Sagittarius trailing tidal tail is

positioned at a roughly constant distance below the Galactic plane, with the Sgr orbital plane nearly coincidental with the Galactic $X_{GC} - Z_{GC}$ plane.⁸ Majewski et al. (2006, hereafter “MLPP”) noted that because of this orientation, longitudinal proper motions of Sgr trailing debris located sufficiently far away from the South Galactic Pole contain virtually no contribution from Sagittarius motions, and almost entirely reflect the solar motion.

Efforts to measure fundamental dynamical properties of the Milky Way, such as its rotation curve, $\Theta(R)$, are complicated by our Sun's own (poorly known) motion within the Galaxy. Measurements of Θ_{LSR} , the Galactic rotation speed at the solar circle (the *Local Standard of Rest*, “LSR”), vary by 25%, despite many efforts at its determination. The value adopted by the IAU in 1985 of $\Theta_{LSR} = 220 \text{ km s}^{-1}$ (see Kerr & Lynden-Bell 1986) has long represented a reasonable approximation to existing measurements (note, however, that prior to the 1985 IAU adoption of $\Theta_{LSR} = 220 \text{ km s}^{-1}$, the 1964 IAU general assembly adopted 250 km s^{-1} ; see a listing of pre-1985 measurements of Θ_{LSR} in Kerr & Lynden-Bell 1986). Constraints taking into account the ellipticity of the disk have suggested the LSR velocity could be as low as $\sim 180 \text{ km s}^{-1}$ (Kuijken & Tremaine 1994). A similarly low value of $184 \pm 8 \text{ km s}^{-1}$ was found by Olling & Merrifield (1998), who modified previous methods of determining the Oort constants by including radial variations of gas density in their mass modeling of the Galactic rotation curve. Proper motions of Galactic Cepheids from *Hipparcos* (Feast & Whitelock 1997) yield a result of $\Theta_{LSR} = (217.5 \pm 7.0)(R_0/8) \text{ km s}^{-1}$ (where R_0 is the distance from the Sun to the Galactic center; the IAU adopted value is $R_0 = 8.5 \text{ kpc}$), in line with the IAU standard. Using re-reduced *Hipparcos* data (van Leeuwen 2007) with improved systematic errors, Yuan et al. (2008) found $\Theta_{LSR} = (243 \pm 9)(R_0/8) \text{ km s}^{-1}$ based on thin-disk O-B5 stars. Estimates based on absolute PMs of Galactic bulge stars in the field of view of globular cluster M4 using the *Hubble Space Telescope* (*HST*) yield $(202.4 \pm 20.8)(R_0/8) \text{ km s}^{-1}$ (Kalirai et al. 2004) and $(220.8 \pm 13.6)(R_0/8) \text{ km s}^{-1}$ (Bedin et al. 2003) (with both studies using data from the same *HST* observations). Long-term *VLBA* monitoring of Sgr A*, the radio source at the Galactic center, led to a proper motion of Sgr A* from which Reid & Brunthaler (2004) revised the LSR velocity upward to $(235.6 \pm 1.2)(R_0/8) \text{ km s}^{-1}$. Ghez et al. (2008) combined stellar kinematics near the Galactic center with the proper motion of Sgr A* to derive $(229 \pm 18)(R_0/8.4) \text{ km s}^{-1}$. More recently, Θ_{LSR} has been suggested to be even higher, $(254 \pm 16)(R_0/8.4) \text{ km s}^{-1}$, based on trigonometric parallaxes of Galactic star-forming regions (Reid et al. 2009). Reanalysis of these same data, including the Sgr A* proper motion, by Bovy et al. (2009) found a similar $(244 \pm 13) \text{ km s}^{-1}$. Koposov et al. (2010) provided constraints on the MW halo potential by analysing the GD-1 (Grillmair & Dionatos 2006) stellar stream, combining SDSS photometry, USNO-B+SDSS proper motions (see Munn et al. 2004, 2008), and spectroscopy to obtain 6-D phase-space data

over a large stretch of the stream, which they used to estimate $\Theta_{LSR} = (224 \pm 13)(R_0/8.4) \text{ km s}^{-1}$ (though this result is made somewhat more uncertain due to a systematic dependence on the flattening of the disk+halo potential). Finally, a combined estimate including many of the above results as priors finds a value of $(236 \pm 11)(R_0/8.2) \text{ km s}^{-1}$ (Bovy et al. 2009). Most of the estimates discussed here rely on the Oort constants, and thus are dependent on our incomplete knowledge of R_0 . Despite numerous attempts at determining the circular velocity at the solar circle, this constant remains poorly constrained. It is clear that independent methods would be valuable to obtain alternative estimates of Θ_{LSR} .

Here we use a new, independent method for ascertaining Θ_{LSR} that has the advantage over most of the previously mentioned methods in that the results have virtually complete decoupling from an assumed value of R_0 . As discussed in MLPP, the trailing arm of the Sagittarius tidal stellar stream is ideally placed to serve as an absolute velocity reference for the LSR. With an orbital pole of $(l_p, b_p) = (274, -14)^\circ$, Sgr is almost on a polar orbit, and the line of nodes of the intersection of the Galactic midplane and the Sgr debris plane is almost coincident with the Galactic X_{GC} axis (the axis containing the Sun and Galactic center). This is illustrated in Figure 2, which shows the projection of Sgr debris from the LM10 model onto the Galactic $X_{GC} - Z_{GC}$, $Y_{GC} - Z_{GC}$, and $X_{GC} - Y_{GC}$ planes. In the upper left panel (the $X_{GC} - Z_{GC}$ plane), the Sgr orbital plane is nearly face-on, while in the other two panels, few Sgr debris points are seen more than $\sim 5 \text{ kpc}$ on either side of the $X_{GC} - Z_{GC}$ plane (i.e., $|Y_{GC}| \lesssim 5 \text{ kpc}$ for nearly all Sgr debris). The motions of Sgr stars *within* its (virtually non-precessing; Johnston et al. 2005) debris plane, as observed from the LSR, are therefore almost entirely in the Galactic U and W velocity components (i.e., in the $X_{GC} - Z_{GC}$ plane), whereas V motions of Sgr tidal tail stars almost entirely reflect *solar motion* — i.e., Θ_{LSR} (plus the Sun's peculiar motion in V , established to be in the range $\sim +5$ to $+12 \text{ km s}^{-1}$; e.g., Dehnen & Binney 1998). The Sgr trailing tail is positioned fairly equidistantly from the Galactic disk for a substantial fraction of its stretch across the Southern MW hemisphere (Majewski et al. 2003). This band of stars arcing almost directly “beneath” us within the $X_{GC} - Z_{GC}$ plane (see the upper panel of Figure 2) provides a remarkable, stationary zero-point reference against which to make direct measurement of the solar motion *almost completely independent of the Sun's distance from the GC*.

Because of the fortuitous orientation of the Sgr debris, the majority of Θ_{LSR} motion (i.e., V) is seen in the proper motions of these stars, with the reflex solar motion almost entirely contained in the $\mu_l \cos(b)$ component for Sgr trailing arm stars (at least for those stream stars away from the South Galactic Pole (SGP) coordinate “discontinuity”, where the $\mu_l \cos(b)$ of Sgr stream stars switches sign). Fig. 4 of MLPP shows the essence of the proposed experiment via measurement of $\mu_l \cos(b)$ for Sgr trailing arm stars, which shows a trend with debris longitude, Λ_\odot^9 , that reflects the solar motion. In the region from $100^\circ \lesssim \Lambda_\odot \lesssim 200^\circ$, $\mu_l \cos(b)$ is nearly constant, because the motion of Sgr debris contributes little to the V -component of velocity. Thus accurate measurement of $\mu_l \cos(b)$ for Sgr trailing tail stars along this stretch of the stream will provide a means of estimating Θ_{LSR} with almost no dependence on R_0 .

⁸ Throughout this paper, when we refer to Galactic Cartesian $(X, Y, Z)_{GC}$ coordinates, we are specifically referring to a right-handed Cartesian frame centered on the Galactic center, with X_{GC} positive in the direction from the Sun to the Galactic center, Y_{GC} in the direction of the Sun's motion through the Galaxy, and Z_{GC} upward out of the plane. Assuming the Sun is at $R_0 = 8.0 \text{ kpc}$ from the Galactic center, this places the Sun at $(X, Y, Z)_{GC} = (-8.0, 0, 0) \text{ kpc}$. The corresponding velocity components will be denoted $(U, V, W)_{GC}$, where the “GC” denotes velocities relative to the Galactic rest frame.

⁹ Λ_\odot was defined by Majewski et al. 2003 as longitude in the Sgr debris plane as seen from the Sun; $\Lambda_\odot = 0^\circ$ at the present Sgr position, and increases along the trailing tail.

Five of the Kapteyn fields for which we have precise (~ 1 mas yr $^{-1}$) proper motions lie squarely on the Sgr trailing arm in this Λ_{\odot} range, and one other (SA 92) is on the periphery of the stream. In Section 4.2, we will use the mean Sgr debris proper motions derived in four of these six fields to derive constraints on Θ_{LSR} .

1.3. Metallicities and Detailed Abundances of the Sagittarius System

Chou et al. (2007) presented one of the first studies of high-resolution spectroscopic metallicities derived for Sgr debris. Their work showed that M-giants along the Sagittarius leading stream exhibit a significant metallicity gradient (which had previously been suggested to be present over smaller separations from the Sgr core based on photometric techniques; e.g., Alard 2001; Martínez-Delgado et al. 2004; Bellazzini et al. 2006), decreasing from a mean $[\text{Fe}/\text{H}] = -0.4$ in the core to ~ -0.7 between ~ 60 – 120° from the core (i.e., between $300 > \Lambda_{\odot} > 240^\circ$), and to ~ -1.1 at $\gtrsim 300^\circ$ from the main Sgr body. Such a population gradient along the stream likely arose due a strong metallicity gradient being present in the dSph before its tidal disruption; thus the outer, more metal-poor populations were preferentially lost as tidal stripping progressed at earlier times relative to the more intermediate-age (and higher metallicity) populations remaining in the core (a mechanism for this process has been demonstrated in the context of an N -body model by LM10). In addition, apparently some younger populations were formed even after Sgr began disrupting. The existence of a population gradient has also been seen by Bellazzini et al. (2006), who found that the relative numbers of blue horizontal branch (BHB) stars to red clump (RC, or red horizontal branch) stars are much higher in a leading stream field than in the Sgr core. Since BHB stars arise in older, more metal-poor populations than the RC stars, this must indicate that the stripped population was made up of predominantly older, less-enriched stars than remain in the core today. Keller et al. (2010) extended the search for chemical evolutionary signatures to the trailing tail of Sgr, observing a handful of stars selected from the 2MASS M-giant catalogs of Majewski et al. (2003) at high resolution in each of two fields at distances of 66° and 132° from the core. Keller et al. combined the mean metallicities in these two fields with the $[\text{Fe}/\text{H}] = -0.4$ result for the Sgr core from Monaco et al. (2005), and derived a metallicity fit as a function of Λ_{\odot} of $\Delta[\text{Fe}/\text{H}] = (-2.4 \pm 0.3) \times 10^{-3}$ dex degree $^{-1}$. This trend (seen in their Figure 4) also passes through the mean metallicity of $[\text{Fe}/\text{H}] \approx -0.6$ derived by Monaco et al. (2007) in a narrow region centered at $\Lambda_{\odot} = 100^\circ$.

For consistency, all of the data included in the Keller et al. (2010) study (including those from Monaco et al. 2005, 2007 and Chou et al. 2010) were derived from M giants, which are, however, biased toward metal-rich, and therefore relatively younger, stars. In the current study, we explore the metallicity in fields between $75 < \Lambda_{\odot} < 130^\circ$ from the Sgr core along the trailing tail using predominantly main sequence stars. Such stars near the main sequence turnoff are much less prone to metallicity biases than M giants, because MSTO stars are present in all stellar populations. An additional advantage of focusing on MSTO stars is that the number density of turnoff stars is much higher than both young, M giant tracers and older horizontal-branch stars; this provides us a much larger sample with which to characterize the Sgr trailing tail metallicity. Older trailing debris populations have recently

been studied by Sesar et al. (2010), who used SDSS Stripe 82 data to develop a new technique for estimating metallicity from photometric data where both RR Lyrae variables and main-sequence stars from the same structure can be identified. Their work found a constant $[\text{Fe}/\text{H}] = -1.20 \pm 0.1$ for Sgr debris along much of the same region of the trailing tail we are studying. In Section 5 we explore the Sgr trailing tail metallicity based on our samples of predominantly MSTO stars.

An important diagnostic of the star-formation timescale in a system is the α -element abundance; the α elements (e.g., Mg, Ca, Ti) are produced mainly in Type II supernovae (SNe), which are the evolutionary endpoints of massive stars that dominate the chemical evolution at early times. Once Type Ia SNe begin to occur, the $[\alpha/\text{Fe}]$ ratio will decrease, because α -elements are less effectively produced by these supernova progenitors, while the overall metallicity, $[\text{Fe}/\text{H}]$, will continue to increase. This produces a “knee” in the $[\alpha/\text{Fe}]$ vs. $[\text{Fe}/\text{H}]$ diagram, which acts essentially as a chronometer for a given system, since the $[\text{Fe}/\text{H}]$ of the knee indicates the transition from SNII-dominated evolution to SNIa contributions. This phenomenon has been seen in a number of dSph systems, which typically show lower $[\alpha/\text{Fe}]$ at a given $[\text{Fe}/\text{H}]$ than Galactic populations because of a slower enrichment (e.g., Shetrone et al. 2001, 2003; Venn et al. 2004; Tolstoy et al. 2003; Geisler et al. 2005; see also a recent review by Tolstoy et al. 2009). However, at the lowest metallicities, the $[\alpha/\text{Fe}]$ of dSphs more closely resemble those of the MW halo. Studies by Sbordone et al. (2007) and Monaco et al. (2005) found the same underabundance of α -elements relative to the Milky Way for the core of the Sagittarius dSph. This finding has been extended into the Sgr trailing stream by Monaco et al. (2007), and into the leading arm by Chou et al. (2010), with both studies using M-giants from the catalog of Majewski et al. (2003). However, M giants are biased to higher metallicity and more recently star-forming population(s) of Sgr, so a natural next step in understanding the evolution of the original, pre-disruption Sgr dSph is to derive detailed abundances (especially for s-process and α -elements) for a significant sample of the more metal-poor, older stars populating the core or, more accessibly, in Sgr’s more nearby streams. In Section 5 we present relative Mg abundances derived from our spectra. We show that the majority of confirmed old, metal-poor Sgr stream members appear to have distinct Mg abundances from those of the Milky Way stellar populations along the lines of sight probed.

1.4. Goals of This Paper

Here, we present data in six of the Kapteyn’s Selected Areas from our deep proper-motion survey (Casetti-Dinescu et al. 2006). In these six fields intersecting the trailing tidal tail of the Sgr system, we have augmented our proper-motion catalogs with follow-up spectroscopy. Sgr debris has been identified from among the stars with measured radial velocities, and these Sgr candidates are used to derive the mean three-dimensional kinematics and chemistry of the Sgr trailing stream.

In Section 2.2, we briefly introduce the proper motion survey (a more detailed discussion of the survey appears in Casetti-Dinescu et al. 2006), and discuss in depth the spectroscopic observations with the WIYN+Hydra and MMT+Hectospec multifiber instruments that yielded a total of > 1500 radial velocities among proper motion-selected stars within the six fields of view. Section 2.3 will detail the final selection of candidate Sgr debris in each of our

fields based on RV, proper motion, and color-magnitude selection. Section 3 presents maximum-likelihood estimates of the most precise proper motions ($\sim 1-2$ mas yr $^{-1}$ per star, or $\sim 0.2-0.7$ mas yr $^{-1}$ mean for each field) yet measured for Sagittarius debris. These measured kinematics are compared to the models of Law & Majewski (2010a), and found to agree rather well with the predictions for Sgr debris motions. However, we follow in Section 4 with an analysis of the residual *disagreement* between our measurements and the models, or more accurately, we use the discrepancy to reassess the magnitude of the solar reflex motion, which is the dominant contributor to the proper motions in the direction of Galactic longitude. We show that our proper motion data (specifically, $\mu_l \cos b$) are inconsistent with the standard IAU value of 220 km s $^{-1}$ for the Local Standard of Rest motion at the $\sim 1-2\sigma$ level and favor a significantly higher value, consistent with several of the most recent Θ_{LSR} studies using radio techniques. In Section 5 we apply a software pipeline designed to derive stellar abundances from low-resolution spectra to the numerous spectra we have obtained for this project. While the metallicities show a hint of a gradient among the metal-poor stars in our study consistent with previous work, we cannot rule out a constant $[\text{Fe}/\text{H}]$ over the range of stream longitude covered. We also examine the relative magnesium and iron index strengths for information on α -abundance patterns of Sgr debris. We find Mg abundances of Sgr members are typically lower at a given $[\text{Fe}/\text{H}]$ than field stars, consistent with the behavior seen in most MW dSphs. Finally, Section 6 concludes with a brief summary of our work, and future avenues these data can be used to explore.

2. THE DATA

2.1. Field Locations

The data discussed here are part of our ongoing deep proper-motion survey in a subset of Kapteyn’s Selected Areas (Majewski 1992; Casetti-Dinescu et al. 2006) at declinations of $\pm 15^\circ$ and 0° . The survey as designed by Kapteyn (1906) consists of $\sim 1^\circ$ fields evenly spaced at $\sim 15^\circ$ intervals along strips of constant declination (see Fig. 1 in Casetti-Dinescu et al. 2006). A handful of our near-equatorial survey fields (see the left panel of Figure 1) fall on or near the location of Sgr trailing tidal debris as mapped by Majewski et al. (2003) using M-giants from 2MASS. The location of our fields relative to the models (constrained by the Majewski et al. data, among others) of Law & Majewski (2010a) can be seen in the right panel of Figure 1, which suggests that we can expect a significant contribution from Sgr debris to the stellar populations along these lines of sight. In Casetti-Dinescu et al. (2006) and Casetti-Dinescu et al. (2008) we showed that faint (V or $g \gtrsim 20$), blue ($B-V < 0.8$ or $g-r < 0.6$) overdensities (at colors and magnitudes consistent with the expected Sgr main sequence turnoff) in the color-magnitude diagrams of those SA fields intersecting the Sgr orbital path also show clumping in the distributions of their proper motions; these excesses and their clumping in proper motion space suggest that a distant, common-motion population, likely to be Sgr tidal debris, is present in these fields. In this work, we focus on six fields: SAs 116, 117, 92, 93, 94, and 71 (listed in order of increasing Λ_\odot). Coordinates for these fields are given in Table 1, which includes equatorial and Galactic positions as well as the longitude and latitude in the Sagittarius coordinate system. In this study, we are discussing fields that are $\sim 74^\circ-128^\circ$ from the core of the Sgr

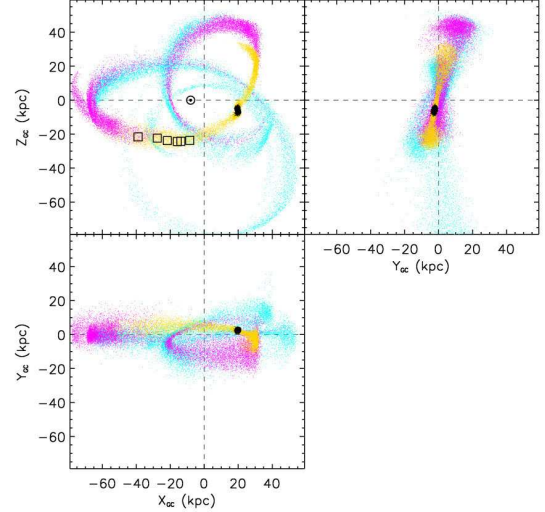


Figure 2. Sagittarius debris from the best-fit triaxial halo model of Law & Majewski (2010a), shown in Galactic $(X, Y, Z)_{\text{GC}}$ (right-handed) coordinates. Colors represent debris stripped on successive orbits, as in Figure 1, with 2 passages of additional (earlier) debris included as cyan points. The three panels represent the projection of Sgr debris onto the Galactic $X_{\text{GC}}-Z_{\text{GC}}$, $Y_{\text{GC}}-Z_{\text{GC}}$, and $X_{\text{GC}}-Y_{\text{GC}}$ planes. In the upper left panel (the $X_{\text{GC}}-Z_{\text{GC}}$ plane) the Sgr orbital plane is nearly face-on; open black squares in this panel denote the positions of the Kapteyn Selected Areas in this study along the Sgr trailing tail. The Sun is represented by the circle at $(X_{\text{GC}}, Z_{\text{GC}}) = (-8.0, 0.0)$ kpc, with the Sgr core (black dots) beyond the Galactic center as viewed from our position, and slightly below the plane. The upper right and lower left panels (i.e., the $Y_{\text{GC}}-Z_{\text{GC}}$ and $X_{\text{GC}}-Y_{\text{GC}}$ planes) illustrate the near-coincidence of the Sgr orbital plane with the Galactic $X_{\text{GC}}-Z_{\text{GC}}$ plane. Note that very few Sgr debris points make excursions of more than $\sim 5-10$ kpc to either side of the Galactic $X_{\text{GC}}-Z_{\text{GC}}$ plane (in the Y_{GC} direction).

dSph, along its trailing stream.

The positions of the SAs in this study in the Galactic Cartesian $X_{\text{GC}}-Z_{\text{GC}}$ plane are shown in the upper left panel of Figure 2, overlaid atop simulated Sgr debris from the LM10 model. Of course, to place points on this figure for the SAs requires an estimate of heliocentric distance. Where needed throughout this work, we use mean distances to Sgr debris in each SA field estimated from the LM10 model debris along corresponding lines of sight. We have chosen to do this rather than measure Sgr debris distances because (a) our data in most fields don’t reach much fainter than the main sequence turnoff of Sgr, and (b) the expected line-of-sight depth of the Sgr stream in this portion of the trailing tail is ~ 10 kpc, which “smears” the main sequence out by as much as ~ 0.5 magnitudes. Both of these factors make isochrone fitting to derive distances rather unconstrained, so for all analysis requiring a distance estimate we adopt the mean model debris distances from LM10 at each position, with the line-of-sight depth of the stream in each field defining the uncertainty in the distance. These values are given in Table 3 below.

2.2. Photometry and Proper Motions

For those fields (SAs 92, 93, 94, and most of SA 116) that lie within the Sloan Digital Sky Survey (SDSS) footprint, we have used photometry (shown in Figure 3) from SDSS Data Release 7 (DR7; Abazajian et al. 2009) for our analyses. The remaining photometric data for this survey (for SAs 71 and 117) are photographic and derived from the late epoch (du Pont 2.5-m telescope) plates from which the proper motions were measured. Calibration of the pho-

Table 1
Kapteyn's Selected Areas in This Study

SA	RA (J2000.0)	Dec (J2000.0)	l (degrees)	b (degrees)	Λ_{\odot} ^a (degrees)	B_{\odot} (degrees)	$E(B-V)$ ^b
71	03:17:11.5	15:24:57.6	167.1	-34.7	128.2	-5.6	0.19
94	02:55:58.1	00:30:03.6	175.3	-49.3	116.3	4.8	0.09
93	01:54:52.1	00:46:40.8	154.2	-58.2	103.2	-3.2	0.03
92	00:55:03.8	00:47:13.2	124.9	-62.1	90.1	-10.6	0.03
117	01:17:04.1	-14:11:13.2	149.0	-75.7	87.6	5.1	0.02
116	00:18:08.4	-14:19:19.2	90.1	-75.0	74.9	-1.4	0.02

^aCoordinates in the Sagittarius system as defined by Majewski et al. (2003). Λ_{\odot} and B_{\odot} are analogous to Galactic longitude and latitude, but rotated such that the Sgr core defines the center of the system (i.e., $\Lambda_{\odot}, B_{\odot} = 0^{\circ}, 0^{\circ}$), with Λ_{\odot} increasing along the trailing tidal tail. The fields in this study sample the trailing tail between $74-128^{\circ}$ from the Sgr core.

^bInterstellar reddening value estimated from the maps of Schlegel et al. (1998).

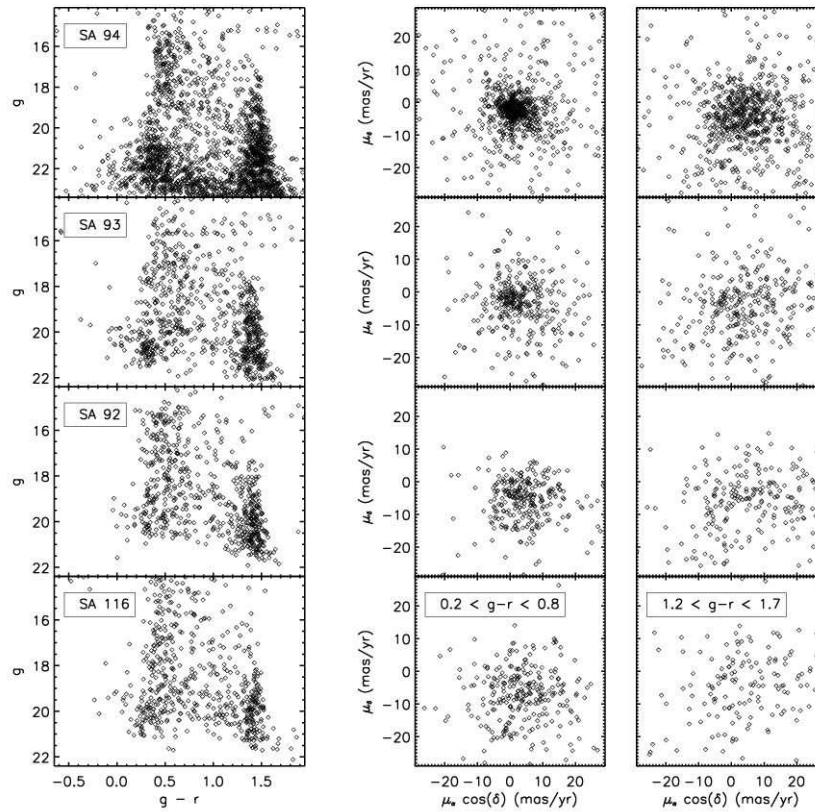


Figure 3. *Left:* SDSS color-magnitude diagrams (CMDs) of all stars with measured proper motions in the four fields of our survey that overlap the SDSS footprint. Each of these CMDs shows the blue ($g-r \sim 0.5$) swath of stars at the bright end made up of primarily Milky Way thin- and thick-disk MSTO stars. Below this feature at similar blue, ($g-r \lesssim 0.6$) colors, but at fainter ($g \gtrsim 19.5$) magnitudes in each field is an apparent overdensity likely made up of Sagittarius main-sequence stars. Note that the much deeper proper motion catalog of SA 94 samples much more of the Sgr main sequence than those catalogs for the other fields. *Right:* Proper motion vector point diagrams (VPD), separated into a blue ($0.2 < g-r < 0.8$) sample (middle column) and a red ($1.2 < g-r < 1.7$) subset (right). Red stars from the prominent feature visible at red colors ($g-r \gtrsim 1.2$) in each CMD should be primarily nearby Galactic M-dwarfs. The blue stars contain main sequence turnoff stars of MW populations, as well as candidate Sgr MSTO stars. The proper motions of many stars are tightly clumped in the blue samples, suggesting that a distant, common-motion stellar population (i.e., Sgr debris) may be present among these stars.

tographic magnitudes in the blue (IIIa-J+GG385) and visual (IIIa-F+GG495) passbands onto the standard Johnson-Cousins system was achieved using CCD photometry taken in 1997-1998 with the Swope 1-m at Las Campanas Observatory. However, that UBV CCD photometry only covers a small portion ($\sim 20-30\%$) of each field, and is shallower than the magnitude limit of the photographic plates by 1-1.5 magnitudes for red stars, and ~ 0.3 magnitudes for blue

stars, yielding poor photometric calibration (for details, see Casetti-Dinescu et al. 2006). Thus, for SAs 71 and 117, those aspects of our analysis that rely on the photometry (e.g., spectroscopic target selection, photometric parallax distance estimates, and calibration of color-dependent systematics in the proper motions) are subject to the uncertainties in calibration of the photographic photometry propagated by up to 0.05 magnitudes in the B and V photometry.

Details of the proper motion reductions appear in Casetti-Dinescu et al. (2006), so here we provide only an overview. For all of the near-equatorial ($-15^\circ \leq \delta \leq 15^\circ$) Selected Areas in our study, proper motions are derived from plates taken with the Mt. Wilson 60-inch between 1909-1912, combined with deliberately matched plates (in approximate area and plate scale) taken by S. Majewski with the 2.5-m Las Campanas du Pont telescope between 1996-1998. All plates were digitized with the Yale PDS microdensitometer. Most background QSOs and galaxies are near the limiting magnitude of the proper motion catalogs derived from solely the Mt. Wilson and du Pont plates; therefore if we used only these data, the correction to an absolute proper motion frame would be determined by only a handful of poorly-measured faint objects. To extend the proper motion limiting magnitude beyond the limit imposed by the Mt. Wilson plates, we augmented the Kapteyn survey data with measurements of plates from the first Palomar Observatory Sky Survey (POSS-I), which were taken in the early 1950s. These plates, while of much coarser plate scale ($67''.2 \text{ mm}^{-1}$; compare to $10''.92 \text{ mm}^{-1}$ for the du Pont, and $27''.12 \text{ mm}^{-1}$ for the 60"), are deeper than the 60" plates, and provide a ~ 40 -year baseline with both the Mt. Wilson plates and the du Pont plates, allowing us to extend the limiting magnitude of the survey (at least for the POSS-I/du Pont proper motion baseline) to $V \gtrsim 20.5$.

In addition, for two of the SA fields in this study (SAs 71 and 94) we have included plates from the Kitt Peak National Observatory Mayall 4-meter telescope, taken at prime focus in the mid-1970s by A. Sandage and in the mid-1990s by S. Majewski. This additional high-quality plate material extends the limiting magnitude in SAs 71 and 94 to $\sim 50\%$ completeness at SDSS r magnitudes of ~ 22 (compared to $\sim 50\%$ completeness at $r \sim 19.5$ in fields without 4-meter plates; the difference in depth between SA 94 and the other fields can be seen in Figure 3). The precision of the proper motion measurements for the "deeper" fields (i.e., those with 4-meter plates) is improved by roughly a factor of 2 at the same magnitude over those with no 4-m plate material; this arises because of both more plate material with fine ($18''.6 \text{ mm}^{-1}$) plate scale at intermediate epochs and the increased depth provided by the 4-m plates.

2.3. Radial Velocities

The survey fields in which we focus this Sgr study fall on or near the portion of the trailing stream in which Majewski et al. (2004) and Monaco et al. (2007) have identified a clear Sgr radial velocity signature. These fields can be seen relative to the orbital path of the Sgr dSph in the left panel of Figure 1, and with respect to the expected location of Sgr trailing tidal debris according to the best-fitting models of Law & Majewski (2010a) in the right panel of Figure 1. We have already shown evidence (Casetti-Dinescu et al. 2006, 2008) that the overdensities of faint, blue stars that are tightly clumped in proper motions in a few of these fields are likely made up of Sgr debris. It was these apparent overdensities that guided our target selection for spectroscopic follow-up. We began with spectroscopy from the Hydra multifiber spectrograph on the WIYN 3.5-m telescope; in most of the shallower fields of this survey, moderate-resolution spectra can be obtained with this instrument in a reasonable amount of observing time. For the deep fields (and some of the shallower fields as well), we used another multi-object spectrograph, the Hectospec instrument on the MMT 6.5-m, which allowed us to observe $\gtrsim 200$ Sgr

stream candidates simultaneously per setup down to faint (g or $V \gtrsim 21.5$) magnitudes. We describe the observations and data reduction for each instrument separately below.

2.3.1. Sample Selection

Targets for spectroscopic follow-up were selected to lie within the locus of the suspected Sgr main sequence turnoff (MSTO) at faint (g or $V \gtrsim 19.5$) magnitudes and blue ($g-r$ or $B-V \lesssim 0.8$) colors. Casetti-Dinescu et al. (2006) showed that the proper motions of these Sgr MSTO candidates clump more tightly than those of the predominantly nearby M-dwarfs at red colors. The tight clumping in the proper motion vector point diagram (VPD) of stars in the MSTO feature was used to define a selection box in proper motion space which should contain any Sgr debris that is present in each field, and eliminate a good fraction of unrelated stars of similar color and magnitude. Care was taken not to be too stringent with either the proper motion or photometric criteria, to preserve as many potential Sgr stars in the wings of the distributions as possible. Because the quality and depth of the photometry and proper motions varies between fields, different candidate selection criteria were adopted for each field.

For WIYN+Hydra observations, only stars brighter than 20th magnitude (either V or g , depending on whether a given field had SDSS photometry) were included in the multifiber setups, because fainter stars than this require rather long exposures with a 3.5-meter telescope to achieve adequate signal-to-noise for radial velocity measurement. After all available fibers were filled with MSTO candidates the remaining fibers were assigned to targets at relatively bright magnitudes ($\lesssim 18$) that also reside within the VPD selection criteria (i.e., potential Sgr RGB stars). Stars fainter than 20th magnitude were targeted with the 6.5-meter MMT telescope, which easily reaches Sgr MSTO candidates in these fields.

2.3.2. WIYN+Hydra Observations

Spectroscopic data were obtained during a total of eight observing runs with the WIYN 3.5-m telescope¹⁰ between December 2002 and November 2008. We used the Hydra multifiber spectrograph in two different setups. The first one (Dec. 2002, Nov. 2003 observing runs) used the 800@30.9 grating with the red fiber cables and an order centered in the neighborhood of the Mg triplet (5170 Å) and covering about 980 Å of the spectrum. This setup delivered a dispersion of 0.478 Å pix^{-1} and a resolving power $R \sim 5400$ (resolution $\sim 1 \text{ Å}$). The second spectrograph configuration (Dec. 2005, Oct./Dec. 2006, Oct./Dec. 2007, and Nov. 2008) used the 600@10.1 grating with the red fiber cable to yield a wavelength coverage $\lambda = 4400\text{--}7200 \text{ Å}$ at a dispersion of 1.397 Å pix^{-1} , for a spectral resolution of 3.35 Å ($R \sim 1500$ at $\lambda = 5200 \text{ Å}$). This spectral region was selected to include the H β , Mg triplet, Na D, and H α spectral features. Typically 60-70 targets were placed on Hydra fibers, with the remaining 15-20 fibers placed on blank sky regions to allow for accurate sky subtraction. Each of the 2005-6 datasets was obtained in less than optimal conditions, including substantial scattered moonlight in Dec. 2005 and cloudy conditions in both 2006 runs. The majority of the 2007 and 2008 data were obtained under favorable conditions. We further note that the Nov. 2008 observing

¹⁰ The WIYN Observatory is a joint facility of the University of Wisconsin-Madison, Indiana University, Yale University, and the National Optical Astronomy Observatory.

Table 2
Summary of Spectroscopic Observations

SA	Date	Telescope/Instrument	Exposures (seconds)	N_{stars}	Mag. limit
71	Dec 2002	WIYN+Hydra ^a	4 x 1800	37	18-19 ^c
-	Nov 2003	WIYN+Hydra ^a	10 x 1800, 4 x 1800	74	18-19
-	Dec 2005	WIYN+Hydra ^b	6 x 1800	27	19.5
-	Oct 2006	WIYN+Hydra ^b	6 x 1800	47	19.0
-	Dec 2006	WIYN+Hydra ^b	4 x 1800	58	19.3
-	Dec 2007	WIYN+Hydra ^b	6 x 2400	53	19.7
-	Dec 2008	MMT+Hectospec	6 x 1800, 6 x 1800	176, 193	22.0
		... TOTAL		503	
92	Oct 2006	WIYN+Hydra ^b	6 x 1800	39	19.4 ^d
-	-	SDSS	-	211	21.5
		... TOTAL		254	
93	Oct 2006	WIYN+Hydra ^b	6 x 1800	55	19.8 ^d
-	Oct 2007	WIYN+Hydra ^b	6 x 1800	51	19.9
-	Dec 2008	MMT+Hectospec	4 x 1500	195	21.5
-	-	SDSS	-	101	21.8
		... TOTAL		292	
94	Oct 2007	WIYN+Hydra ^b	8 x 1800	15	19.0 ^d
-	Dec 2007	WIYN+Hydra ^b	6 x 2400	53	19.9
-	Dec 2008	MMT+Hectospec	8 x 1800, 6 x 1800	189, 165	22.5
-	-	SDSS	-	88	22.5
		... TOTAL		432	
116	Oct 2007	WIYN+Hydra ^b	6 x 1800	25	16.7 ^d
-	Dec 2007	WIYN+Hydra ^b	4 x 2700	59	17.7
-	Nov 2008	WIYN+Hydra ^b	7 x 1800	60	19.9
		... TOTAL		122	
117	Oct 2007	WIYN+Hydra ^b	8 x 1800	47	19.6 ^c
-	Dec 2007	WIYN+Hydra ^b	4 x 2400	49	19.7
-	Dec 2008	MMT+Hectospec	(4 x 1800)+(4 x 1500)	182	20.5
		... TOTAL		206	

^aThese WIYN+Hydra observations used the 800@30.9 grating with the red fiber cables, centered at ~ 5200 Å, yielding ~ 1.0 Å resolution spectra.

^bThese WIYN+Hydra observations used the 600@10.1 grating with the red fiber cables, yielding spectra covering wavelengths from $\sim 4400 - 7200$ Å at ~ 3.35 Å resolution.

^c"Roughly calibrated" V magnitudes (see Casetti-Dinescu et al. 2006).

^dSDSS g magnitude.

run occurred after the WIYN Bench Spectrograph Upgrade, which included the implementation of a new collimator into the Bench configuration, as well as a new CCD that delivers greatly increased throughput.

Table 2 summarizes the observations. Each Hydra configuration was exposed multiple times (usually in sets of 30 min. exposures) to enable cosmic ray removal. Standard pre-processing of the initial two-dimensional spectra used the CCDRED package in IRAF.¹¹ Frames were summed, then 1-D spectra were extracted using the DOHYDRA multifiber data reduction utilities (also in IRAF). Dispersion solutions were fitted using 30–35 emission lines from CuAr arc lamp exposures taken at each Hydra configuration. On each observing run we targeted a few bright radial velocity standards covering spectral types from F through early K (both dwarfs and giants), each through multiple fibers, to yield multiple individual cross-correlation template spectra. These RV stan-

dard spectra were cross-correlated against each other using the IRAF tool FXCOR to determine the accuracy of the velocities and remove any outliers (i.e., those stellar spectra that yield unreasonable cross-correlation results due to template mismatch or some defect, such as a poorly-removed cosmic ray, bad CCD column, or other unknown culprit). Measured velocities of the RV standards typically agreed with published IAU standard values to within 1-2 km s⁻¹. Radial velocities for program stars were derived by cross-correlating all object spectra against all of the standards taken on the same observing run. To maximize the S/N in faint, metal-poor stars, only ~ 200 Å-wide regions centered on the H β , Mg triplet, and H α absorption lines were used for cross-correlation.

Radial velocity uncertainties were derived using the Vogt et al. (1995) method, as described in Muñoz et al. (2006a) and Frinchaboy et al. (2006). The Tonry-Davis ratio (TDR; Tonry & Davis 1979) scales with S/N , such that individual RV errors can be calculated directly from the TDR, provided you have multiple observations at varying S/N of some particular standard star to map the dependence. We have used this technique for all datasets except those from

¹¹ IRAF is distributed by the National Optical Astronomy Observatory, which is operated by the Association of Universities for Research in Astronomy (AURA) under cooperative agreement with the National Science Foundation.

the Dec. 2006 observing run, when only a total of four RV standard spectra were taken. For the SA 71 configuration observed on this run, the RV uncertainty for each star is derived as the standard deviation of the RV results from that star's spectrum using cross-correlation against each of the four standards. Typical RV uncertainties for individual measurements for all fields were $\sigma_V \approx 5 - 10 \text{ km s}^{-1}$, with most spectra having $S/N \sim 15 - 20$ per Angstrom. The uncertainty depends on S/N (essentially magnitude) for all stars from a single Hydra pointing; however, the varying exposure times between Hydra setups and changing observing conditions mean that σ_V is not strictly a function of magnitude in our final catalogs.

2.3.3. MMT+Hectospec Observations

To obtain spectra of fainter Sgr MSTO candidates, we were granted three nights of queue-scheduled NOAO observing time on the MMT 6.5-m.¹² A total of six observing configurations were observed with the 300-fiber Hectospec multifiber spectrograph (Fabricant et al. 2005) mounted at the f/5 focus of the MMT. Targets were selected from among the apparent stellar overdensities of blue MSTO candidates at magnitudes too faint ($g \gtrsim 20$) to be reasonably observed with WIYN+Hydra, but using the same proper motion criteria used to choose Hydra targets. In each of these configurations, a few targets previously observed with Hydra were included for a radial velocity consistency check, and any fibers unable to be filled with faint stars were assigned to brighter ($g < 20$) Sgr RGB candidates.

We used the 270 gpm grating, centered at $\sim 6400 \text{ \AA}$, to give a working wavelength range of 3700-9150 \AA at a dispersion of $\sim 1.21 \text{ \AA pix}^{-1}$ (4.85 \AA resolution). This low resolution allows us to obtain adequate signal-to-noise ($S/N \gtrsim 10$ per \AA) spectra of stars as faint as $g = 22.5$ to measure radial velocities in 3-4 hours of total exposure time. We observed two multifiber setups each in SAs 71 and 94, the two fields in this study that have 4-meter plates (and thus deeper proper-motion catalogs). The rest of the time was devoted to one configuration each in SAs 93 and 117. Each configuration had 200-230 targets assigned (essentially as many as the fiber assignment software would allow), with the remainder designated as sky fibers. The sky fibers were chosen in areas with the nearest $g < 22$ star at least $15''$ away, distributed throughout the field so that a number of them would fall within each of the two CCD chips of the Hectospec system. The number of exposures in each field, each exposure time, the number of stars with measured radial velocities, and the limiting magnitude of each spectroscopic field are given in Table 2.

The Hectospec data were reduced using an external version of the SAO "SPECROAD" reduction pipeline (Mink et al. 2007) written by Juan Cabanela and called ESPECROAD.¹³ The pipeline automates many reduction steps, including bias-correction, flat-fielding, cosmic-ray rejection, fiber-to-fiber throughput adjustments, and sky subtraction. Wavelength calibration was performed manually using sets of three combined HeNeAr calibration lamp exposures from each night of observing.

We derived RVs using the IRAF task FXCOR to cross-

correlate object spectra against fourteen template RV standard spectra of nine different stars ranging in spectral type from F through K. We first correlated the standard spectra against each other, and found that our measurements agree with published RVs¹⁴ to within 4.9 km s^{-1} for all of these stars, with zero mean offset, and $\sigma_{\Delta V} = 3.0 \text{ km s}^{-1}$. To minimize the effects of noise for spectra with lower S/N , the cross-correlation was restricted to the regions around the $H\alpha$, Mg triplet, and $H\beta$ lines.

Each of the object spectra was cross-correlated against all 14 standards, and the mean RV from each of these 14 measurements was adopted as the final result. For the queue-scheduled Hectospec observations, we relied on the queue to provide radial velocity standards. We were thus unable to obtain repeated exposures of the same RV standard stars to allow us to use the "Vogt method" (as described in Section 2.3.2) to determine RV errors. Instead, uncertainties were estimated as the standard deviation of the 14 independent RV measurements thus derived, and vary (essentially as a function of S/N) from $\sigma_{V_{\text{helio}}} \sim 3 \text{ km s}^{-1}$ at $g = 18.0$ to $\sim 15 \text{ km s}^{-1}$ at $g = 21.5 - 22$.

From repeat measures of a handful of stars, including multiple Hydra or Hectospec observations as well as many observed with both systems, we found mean systematic offsets of $< 5 \text{ km s}^{-1}$ between observing runs (including both Hydra and Hectospec data). These offsets were applied to all RVs from a given run to place all measurements on the same system as the Dec. 2007 WIYN+Hydra velocities.

We also note that because we selected most Hectospec targets to be faint, blue objects with miniscule proper motions, a large number of obvious QSOs and AGN spectra appeared in our data. These were added to the samples of QSOs and galaxies that provided the fixed absolute proper motion frame in each field, improving the zero points in these fields.

2.3.4. SDSS spectra

We supplemented our database of radial velocities by matching our proper motion catalogs to the SDSS spectroscopic database. The number of additional RVs contributed by SDSS in each field is noted in Table 2. The majority of SDSS stars are red, nearby M-dwarfs, so very few additional Sagittarius candidates were contributed by the addition of these spectroscopic data. However, the handful of Sgr stars that are present, as well as any other stars in common with our observations, were used for a consistency check. From the stars in common between SDSS and our observations in SAs 94 and 93, we find mean offsets of $\leq 5 \text{ km s}^{-1}$. The accuracies of SDSS radial velocities are $\sim 4 \text{ km s}^{-1}$ at $g < 18$, decreasing to $\sim 15 \text{ km s}^{-1}$ at $g \sim 20$ (Yanny et al. 2009a), so we choose not to offset the RVs.

3. SAGITTARIUS TIDAL DEBRIS KINEMATICS

3.1. Radial Velocities

Figure 4 shows all measured velocities in each of the six survey fields (the total number of stellar radial velocities in each field is given in Table 2) in the Galactocentric (V_{GSR}^{15}) frame. These consist of all RVs from WIYN+Hydra,

¹² Observations reported here were obtained at the MMT Observatory, a joint facility of the Smithsonian Institution and the University of Arizona. MMT telescope time was granted by NOAO (proposal ID 2008B-0448), through the Telescope System Instrumentation Program (TSIP). TSIP is funded by the NSF.

¹³ <http://iparrizar.mnstate.edu/~juan/research/ESPECROAD/>

¹⁴ From the Geneva Radial-Velocity Standard Stars at <http://obswww.unige.ch/~udry/std/>

¹⁵ $V_{\text{GSR}} \equiv V_{\text{helio}} + 9.0 \cos b \cos l + 232.0 \cos b \sin l + 7.0 \sin b$, where V_{helio} is the measured heliocentric radial velocity. This calculation assumes a circular velocity of 220 km s^{-1} at the solar circle, and solar peculiar motion of $(U, V, W) = (9.0, 12.0, 7.0) \text{ km s}^{-1}$.

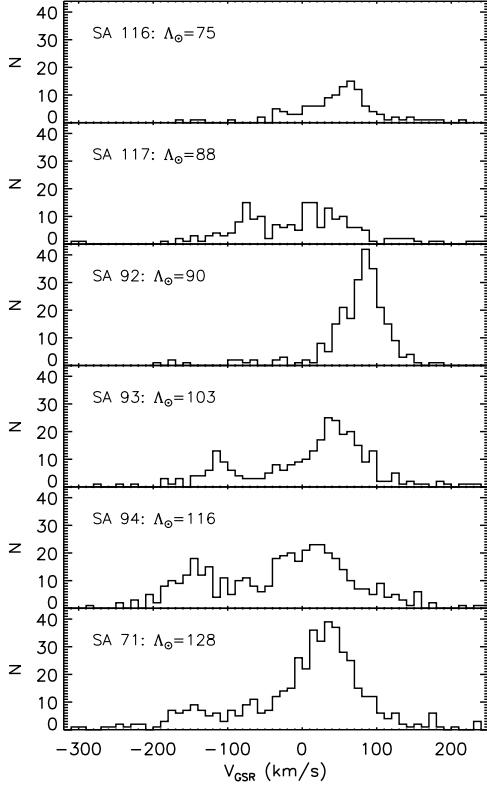


Figure 4. Measured radial velocities (relative to the Galactic Standard of Rest) in each of the six fields, displayed in order (from top to bottom) of Sgr longitude (i.e., angular distance from the Sgr core), Λ_{\odot} . The prominent peak in each field at $V_{\text{GSR}} \sim 0-100 \text{ km s}^{-1}$ is made up primarily of Galactic stellar populations. In SAs 117, 93, 94, and 71, an additional peak at lower velocities is visible. As shown in Section 3, this peak can be attributed to the presence of Sgr tidal debris in these fields.

MMT+Hectospec, and where available, SDSS. Where multiple measurements exist, the final catalog reflects the error-weighted mean radial velocity. In each of these fields, a broad peak is seen at $V_{\text{GSR}} \sim 0-100 \text{ km s}^{-1}$ which is made up primarily of Milky Way stellar populations in these high-latitude fields. An additional velocity peak is evident in SAs 71, 94, 93, and 117, well separated (in all fields except SA 117) from the Galactic distribution in each of these fields; it is this additional peak we shall show to consist of mainly Sagittarius trailing tidal debris. There is no readily apparent peak at lower V_{GSR} values in SAs 92 and 116 – this arises for different reasons in the two cases. SA 116 is the field in which we have the fewest measured radial velocities, and even the stars for which we do have data are not optimally selected to find Sgr debris. Because of limitations on exposure times due to weather, the observed stars were all at relatively bright magnitudes ($g < 18$), where only very few Sgr red giants should be found. More spectra of stars at faint ($g \gtrsim 19$) magnitudes and blue colors will be necessary to identify Sgr debris among the SA 116 data. In SA 92, on the other hand, nearly twice as many spectra are available than in SA 116, and mostly at relatively faint magnitudes. The paucity of obvious Sgr debris in this field is because of the location of SA 92 on the periphery of the stream, where Sgr stellar densities are rather low. There are a handful of stars at low ($V_{\text{GSR}} < 0 \text{ km s}^{-1}$) velocities, but hardly enough candidates to assert that a clear Sgr presence is indicated in SA 92.

To assess whether these apparent velocity overdensities are expected among Galactic populations in each line of sight, we compared the radial velocity distributions to those from the Besançon Galaxy model (Robin et al. 2003).¹⁶ In each SA field, the model query was run five times to smooth out the finite sampling statistics in each individual model run. The five catalogs were concatenated, then for each Kapteyn field the measured velocities were compared to the expected radial velocities of smooth Galactic populations by scaling the summed Besançon model to match the total number of stars in the broad peak in each RV histogram. This was done separately for “bright” and “faint” samples in each field, since stars in different magnitude ranges preferentially sample different Galactic populations with different velocity distributions (e.g., “faint” blue Galactic stars in the region of the CMD where Sgr MSTO stars reside will be predominantly halo stars, and thus have a much higher velocity dispersion than stars of similar color, but much brighter magnitude, where thin/thick disk MSTO stars predominate).

The resulting scaled model distributions are shown as grey filled histograms in Figure 5 for SAs 71 and 94, with the measured heliocentric radial velocities given as solid-lined histograms. The broad peak is reproduced well by the model populations, suggesting that (a) there are no large global velocity offsets present in our data, and (b) the prominent peaks are indeed due to foreground/background Milky Way stars. The additional peaks at $V_{\text{helio}} \approx -170 \text{ km s}^{-1}$ (SA 71) and $V_{\text{helio}} \approx -150 \text{ km s}^{-1}$ (SA 94) are clearly not due to any expected Galactic populations along these lines of sight.

Similar histograms are shown for SAs 93 and 117 in Figure 6, which again clearly show that the broad, prominent peak in each field is made up of Galactic populations, and the peaks at $V_{\text{helio}} \approx -160 \text{ km s}^{-1}$ (SA 93) and $V_{\text{helio}} \approx -100 \text{ km s}^{-1}$ (SA 117) are inconsistent with expected Milky Way velocities. Note that the peak in SA 117 overlaps the wings of the Galactic distribution, making it slightly more difficult to isolate bona fide Sgr members in this field on the basis of radial velocities alone.

Finally, we performed the same examination in SAs 92 and 116, with the results shown in Figure 7. Nearly all of the velocities shown in SA 92 are from the SDSS database, and are predominantly very red M-dwarfs. For this reason, the long tail of the RV distribution at negative velocities, which is due to thick disk and halo MSTO stars, is not well reproduced by our data set. There are a small number of stars at Sgr-like velocities in Figure 7, but these fall within the expected locus of MW stars, so we cannot definitively say that Sgr members are present among our SA 92 sample. In SA 116, no excess peak of measured RVs relative to the model predictions is apparent. This is not surprising given (a) the caveats in the first paragraph of this section regarding the data in SA 116, and (b) the fact that the Law & Majewski (2010a) model predicts Sgr debris in this field to have RVs of $-100 \lesssim V_{\text{helio}} \lesssim -50 \text{ km s}^{-1}$, overlapping the wings of the Galactic distribution in this field. A handful of Sgr members may thus be present among our velocities, but they are difficult to distinguish from the Milky Way halo stars by their RVs.

With RVs in hand, a next culling for Sgr stream candidates was obtained by simply taking all stars within a generously defined range around the evident associated radial velocity peak. Such a selection will include a few Milky Way inter-

¹⁶ Model query available at <http://model.obs-besancon.fr/>.

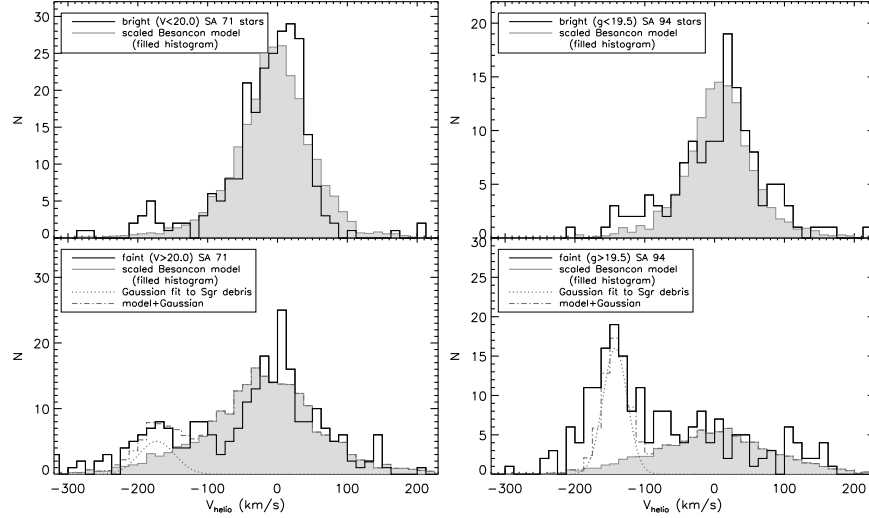


Figure 5. Measured heliocentric radial velocities (solid-line histograms) in SAs 71 (left) and 94 (right), divided into a bright (SA 71: $V < 20.0$; SA 94: $g < 19.5$) sample (upper panels) and a faint (SA 71: $V > 20.0$; SA 94: $g > 19.5$) group (lower panels). The filled gray histogram in each panel is made up of Besançon model points along the corresponding line of sight in the same magnitude ranges as the data histograms, scaled to contain the same total number of stars between $-50 < V_{\text{helio}} < 100 \text{ km s}^{-1}$ as the observed data. In the lower panels, a Gaussian representing the best-fitting radial velocity and dispersion of Sgr candidates is shown (dotted curve), along with the sum of this Gaussian and the Besançon distribution (dot-dashed histogram). These two fields include 4-meter plates in the proper motion derivation, and thus contain the deepest proper motions (and the most Sgr candidates) of any fields in the survey. Very little, if any, Sgr debris is evident in the bright samples.

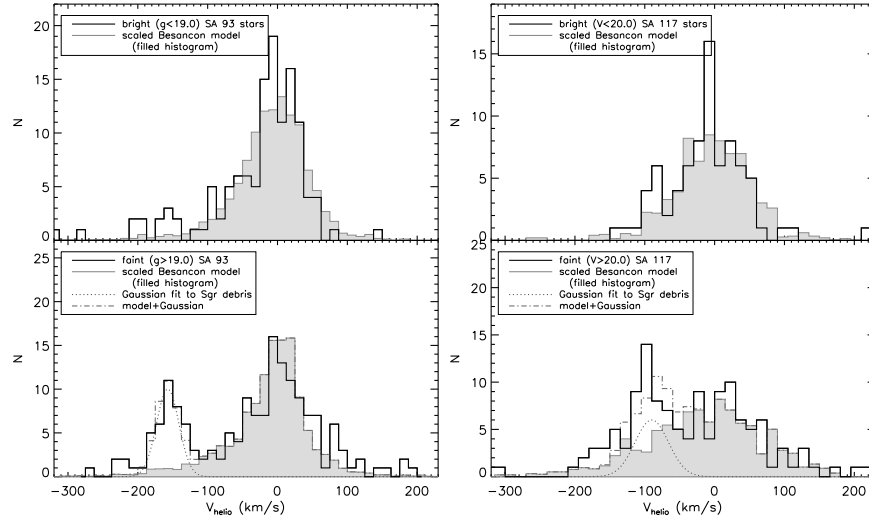


Figure 6. Same as Figure 5, but for SAs 93 (left) and 117 (right), and with slightly different definitions of the bright (SA 93: $g < 19.0$; SA 117: $V < 20.0$) sample (upper panels) and faint (SA 93: $g > 19.0$; SA 117: $V > 20.0$) group (lower panels). In both of these fields, there is a hint of a peak at Sgr-like velocities in the bright samples, suggesting that a few Sgr red giants may have been identified in these fields.

lopers, so we examined the samples thus selected to remove non-Sgr stars. We first removed all stars with proper motions $|\mu| > 10 \text{ mas yr}^{-1}$ in either dimension; such stars, if actually at the distance of the Sgr trailing tail in this region of sky ($\sim 25\text{--}40 \text{ kpc}$), would have unreasonably large ($> 1000 \text{ km s}^{-1}$) tangential velocities ($V_{\text{tan}} = 4.74 d \mu \text{ km s}^{-1}$, where d is the distance in kpc and μ the proper motion in mas yr^{-1}). Faint, blue stars with proper motions of this magnitude must therefore be nearby (foreground) MW white dwarfs or metal-poor subdwarfs. After removing these stars, we then examine the positions of all selected candidates in the color-magnitude diagram. We reject faint stars that are well redward of the read-

ily apparent Sgr main sequence, and at brighter magnitudes, we remove only stars at positions obviously inconsistent with being Sgr red giants or horizontal branch stars. In SA 93, a clear offset was visible between mean proper motions of bright ($g < 19.0$) Sgr candidates and fainter ones, so we chose to keep only candidates at $g > 19.0$, on the assumption that the density of stream stars should be much greater at fainter magnitudes near the lower RGB and MSTO than along the upper RGB. This yields fewer total Sgr candidates, but the ones that remain have much higher probability of being Sgr members than do the brighter candidates.

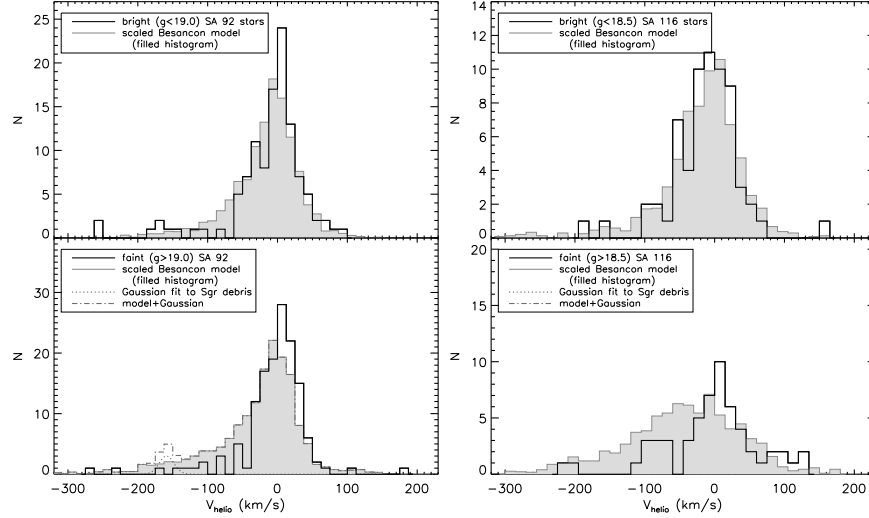


Figure 7. Same as Figure 5, but for SAs 92 (left) and 116 (right), and with slightly different definitions of the bright (SA 92: $g < 19.0$; SA 116: $g < 18.5$) sample (upper panels) and faint (SA 93: $g > 19.0$; SA 117: $g > 18.5$) group (lower panels). No excess peak is evident (relative to the Besançon predictions) in either of these fields, meaning we have likely sampled very few Sgr radial velocity members along these lines of sight.

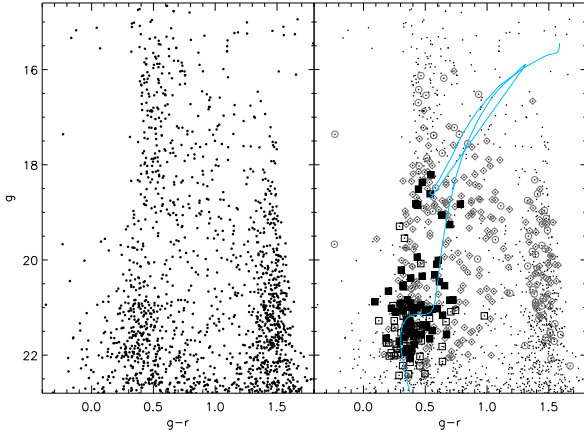


Figure 8. SDSS g vs. $g-r$ CMDs of SA 94; the left panel shows all objects in our proper motion catalog that were flagged as stars by the SDSS star/galaxy separator. The right panel overplots all stars observed spectroscopically as larger symbols: candidates within the initial RV selection are black squares (filled squares: final Sgr candidates; open squares: in RV selection, but removed by other criteria), open diamonds are stars with RVs outside the Sgr RV selection, and open circles are stars that only have RVs in SDSS (note that none of these ended up being selected as Sgr candidates). The final Sgr candidates that we selected by RV, proper motion, and color-magnitude position (filled squares) are concentrated around a likely MSTO of Sgr debris. The blue curve is a Girardi et al. (2004) isochrone for a 10 Gyr population at $[\text{Fe}/\text{H}] = -1.3$ and a distance of 30 kpc.

3.2. Selecting Final Sgr Candidates

We now discuss how we pared down the samples of Sgr candidates from the initial broad RV and proper motion selections in each field to the final, more securely-identified samples used for analysis. For brevity, we will show detailed examples for only two of the six fields in the study. The first of these is SA 94, which is the "best-case" field in our study, because it has deep proper motions due to the availability of 4-meter plates in its data set. For comparison, we follow the SA 94 discussion with details of SA 93, which has a much shallower proper motion catalog than SA 94, but also has high-quality SDSS photometry. These two fields were chosen simply to give the reader an idea of the type and quality

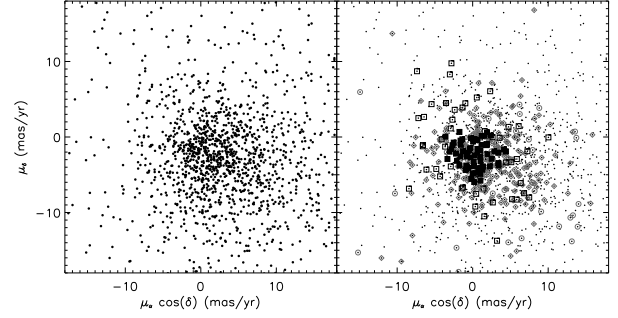


Figure 9. Proper motion vector point diagram of SA 94, with panels and symbols as in Figure 8.

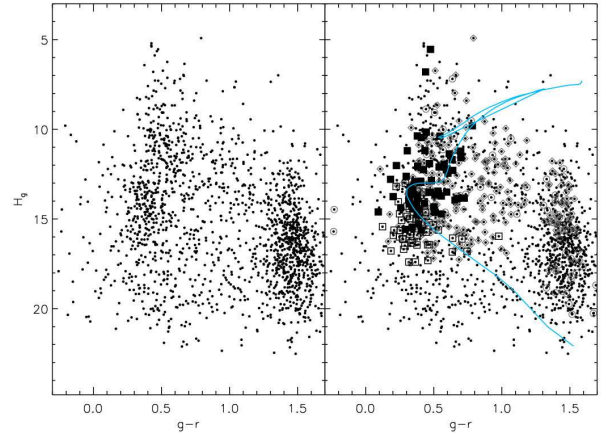


Figure 10. Reduced proper motion diagram (RPMD) for SA 94, where $H_g \equiv g + 5 \log \mu + 5$, with μ in arcsec yr^{-1} . Panels and symbols are as in Figure 8. The blue curve is a Girardi et al. (2004) isochrone for a 10 Gyr population at $[\text{Fe}/\text{H}] = -1.3$ and a distance of 30 kpc, with the measured mean proper motion of Sgr debris in SA 94 ($\mu_{\text{tot}} = 2.34 \text{ mas yr}^{-1}$) used to convert to reduced proper motion.

of the data included in this study, and the process we followed to select Sgr candidates.

3.2.1. Selecting Sgr Candidates in SA 94

Figure 8 shows the SDSS $g-r$ vs. g color-magnitude diagram (CMD) for SA 94. The left panel shows all stars for which we have measured proper motions, with SDSS-classified galaxies removed from the sample. On the right-hand side, open squares depict all stars observed spectroscopically to illustrate the candidate selection. The majority of spectroscopic targets in this deep proper-motion field were selected from the Sgr MSTO feature of faint, blue stars, and observed with the large-aperture MMT 6.5-m telescope. The remaining targets are either (a) bright stars observed with WIYN+Hydra, or (b) targets chosen to fill unused fibers after all possible MSTO candidates had been assigned. The final culled sample of Sgr candidates (based initially on RV selection, with further interactive proper-motion and CMD selection performed as discussed below) is shown by the large, filled black squares. As expected, these concentrate at the Sgr MSTO locus, with a handful of brighter stars having properties consistent with Sgr membership as RGB or red clump stars. We have overlaid an isochrone from Girardi et al. (2004) for an old (10 Gyr), metal-poor ($[\text{Fe}/\text{H}] = -1.3$) population at the expected distance ($d = 29.5$ kpc; Law & Majewski 2010a) of Sgr debris in SA 94; the age and metallicity of this isochrone is chosen to match the Sgr metal-poor population identified by Siegel et al. (2007), which should be the dominant contributor to debris in this portion of the trailing tail. The final set of Sgr candidates in this field concentrate near this ridgeline; most of the scatter about the isochrone is likely due to the ± 5 kpc line-of-sight depth of the Sgr stream as well as the intrinsic population dispersion in Sgr. The proper motion vector point diagram (VPD) is displayed as Figure 9, with panels and symbols the same as in Figure 8. Sgr candidates clump more tightly in the VPD than the overall population of spectroscopic targets, which is consistent with the notion that we are indeed measuring a distant, common-motion grouping of stars.

To further cull the sample, we turn to the reduced proper motion diagram (RPMD). Reduced proper motion, defined as $H_g \equiv g + 5 \log \mu + 5$, where g is the apparent magnitude and μ is the total proper motion in arcsec yr^{-1} , compresses stars with common tangential velocity into coherent features in the RPMD. Thus, a common-motion population should form a sequence in the RPMD, even if the population has a significant line-of-sight depth (see Majewski 1999, especially Figure 4). In Figure 10 we show such a diagram for SA 94, with the same isochrone as in Figure 8, shifted to the measured tangential velocity of SA 94 Sgr debris (to be discussed in Section 3.3). After an initial calculation of the mean motion, candidates that were obviously inconsistent with a broadly-defined region ($\gtrsim 0.3$ magnitudes in H_g and/or $g-r$) about the ridgeline were manually removed from the sample.

3.2.2. Selecting Sgr Candidates in SA 93

SA 94 is one of only two fields (with SA 71) of the six in this study that have KPNO 4-m plates, and thus have 1-1.5 magnitude deeper proper motions. Furthermore, of those two, SA 94 has higher-quality photometry (from SDSS) than the photographic magnitudes used for SA 71. Thus SA 94 is our best field in terms of overall data quality. To illustrate how a more typical field compares to the highest-quality SA 94 data, we show in Figures 11, 12, and 13 the same type of plots as in Figures 8, 9, and 10, but for SA 93. This field is located in a high stellar density region of the stream, as is SA 94, but has

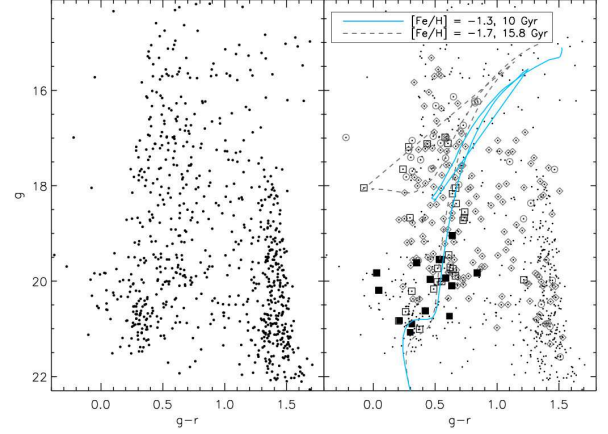


Figure 11. SDSS g vs. $g-r$ CMDs of SA 93, with panels and symbols the same as in Figure 8. Because the proper motion catalog in this field doesn't reach nearly as faint stars as in SA 94, far fewer Sgr candidates have been identified among our radial velocities. Note also that for reasons discussed in the text, only stars with $g > 19.0$ were kept in the final sample. The blue curve is a Girardi et al. (2004) isochrone for a 10 Gyr population at $[\text{Fe}/\text{H}] = -1.3$ and a distance of 28 kpc. To illustrate the possible presence of very old, evolved stars among the Sgr candidates, we also overlay a grey dashed curve for the same distance, but $[\text{Fe}/\text{H}] = -1.7$ and an older (~ 15.8 Gyr) population. Note that many of the open squares (RV candidates not included in the final sample) lie along the asymptotic giant branch of this old, metal-poor population.

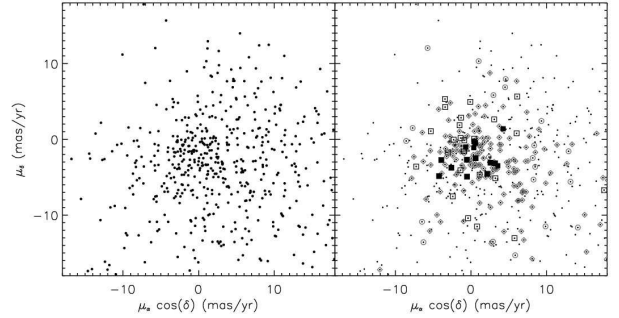


Figure 12. Proper motion vector point diagram of SA 93, with panels and symbols as in Figure 8.

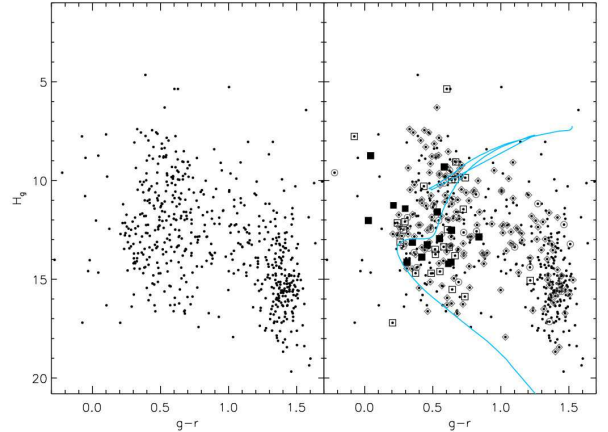


Figure 13. Reduced proper motion diagram (RPMD) for SA 93, where $H_g \equiv g + 5 \log \mu + 5$, with μ in arcsec yr^{-1} . Panels and symbols are as in Figure 8. The blue curve is a Girardi et al. (2004) isochrone for a 10 Gyr population at $[\text{Fe}/\text{H}] = -1.3$ and a distance of 28 kpc, with the measured mean proper motion of Sgr debris in SA 93 ($\mu_{\text{tot}} = 2.69 \text{ mas yr}^{-1}$) used to convert to reduced proper motion.

shallower proper motion data (see Fig. 3), providing far fewer

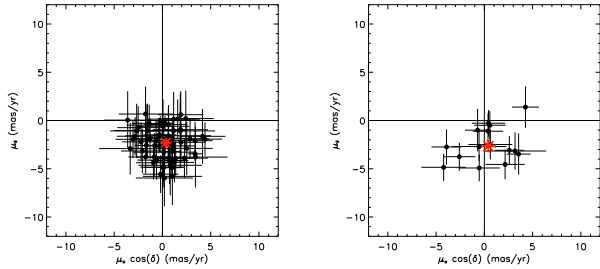


Figure 14. Proper motions of only the final Sgr candidates in SAs 94 (left panel) and 93 (right panel), with individual error bars. In SA 93, a proper motion offset was apparent between faint ($g > 19.0$) candidates and brighter Sgr candidates; for this reason, only the faint candidates were retained. The red asterisks represent the final maximum likelihood estimate of the mean Sgr debris motion in each field.

Sgr MSTO candidates for follow-up spectroscopy. Because the available proper-motion data do not sample the MSTO as robustly as in SA 94, this field was given lower priority for spectroscopy, with only one relatively short MMT+Hectospec configuration observed (see Table 2). However, in this one Hectospec setup, nearly all available $g \lesssim 20.2$ Sgr candidates satisfying the (somewhat relaxed relative to SA 94) target selection criteria were observed. The overlaid Girardi et al. (2004) isochrone for an old (10 Gyr), metal-poor ($[\text{Fe}/\text{H}] = -1.3$) population at the expected distance ($d = 28$ kpc) of Sgr debris in SA 93 (blue curve in Figure 11) is seemingly consistent with all but the brightest of the identified candidates. We have also overplotted (dashed gray curve) an older (~ 15.8 Gyr), more metal-poor ($[\text{Fe}/\text{H}] = -1.7$) isochrone with the same distance as the blue curve; this curve passes through the positions of the bright, blue stars, suggesting that they may also be Sgr members of an old horizontal-branch/asymptotic giant branch population. However, the MSTO of such an old population is beyond the magnitude limit of our proper-motion survey.¹⁷ The RPMD (Figure 13) for SA 93 shows the same ridgeline as in the CMD, shifted by the final measured tangential velocity for the Sgr candidates. Because the uncertainty in the mean proper motion is much larger in this field than in SA 94 (on the order of $\sim 100 \text{ km s}^{-1}$ in tangential velocity for SA 93, compared to $\sim 50 \text{ km s}^{-1}$ in SA 94), it is difficult to conclude much from the RPMD. The benefits of the additional 4-meter plates in SAs 94 and 71 are clearly illustrated by the relatively fewer identified Sgr stream members in the shallower SA 93 field compared to the deeper data sets. Zoomed-in versions of the VPDs for SAs 94 and 93 are given in Figure 14, with error bars shown on all points to illustrate the quality of the proper-motion data (note that the error bars on individual stars in each of the panels of Fig. 14 are of comparable size, in spite of the higher-quality proper motion data in SA 94 than in SA 93, because the majority of Sgr candidates in SA 94 are faint [$g > 21$] MSTO candidates, while SA 93 candidates are mostly > 1 magnitude brighter than this). As previously mentioned, a proper motion offset was seen between faint ($g > 19.0$) stars in SA 93 and brighter candidates; we included only the faint ($g > 19.0$) stars in our proper motion measurement, because these are more likely to be true Sgr members. The maximum likelihood estimate of

the absolute proper motion of Sgr debris in each field is represented by the large red asterisks, which have 1σ uncertainty smaller than the size of the point.

3.2.3. Summary of Sgr Candidate Selection

In summary, the basic Sgr candidate selection in each Selected Area began with a broad RV selection centered on the apparent Sgr velocity peak (e.g., $-250 < V_{\text{hel}} < -100 \text{ km s}^{-1}$ in SAs 94 and 93). This was followed by removing high proper motion stars ($|\mu| > 10 \text{ mas yr}^{-1}$ in either dimension), which would have tangential velocities much greater than the Milky Way escape velocity if those stars were at the 25-40 kpc distances of Sgr debris along the SA lines of sight. We then used our knowledge of the distance and metallicity expected for Sgr debris in these fields to remove stars at faint magnitudes that are more than ~ 0.3 magnitudes from the expected color-magnitude and RPMD loci in each field (note that in some cases we did not apply this at bright magnitudes, since there is considerable uncertainty about the exact CMD locus for Sgr debris above the turnoff). We calculated mean proper motions from the selected stars, then iteratively removed outliers ($> 3\sigma$) in proper motion. Finally, we manually inspected the remaining candidates to remove any stars that were $\sim 1-2\sigma$ outliers from the identified Sgr locus in *all observables* (i.e., RV, $g-r$ color, magnitude, and proper motion).

Once Sgr candidates were selected using color, magnitude, RV, proper motion, and RPMD criteria, the kinematical properties of Sgr debris in each SA field were estimated using a maximum likelihood method (e.g., Pryor & Meylan 1993; Hargreaves et al. 1994; Kleyna et al. 2002). The final measured radial velocities and velocity dispersions, along with uncertainties in these values, are given in Table 3 in both the heliocentric and Galactocentric (GSR) frames. The estimates of the mean radial velocity (in the GSR frame) of Sgr debris can be seen in the top panels of Figure 15, which overlays our measurements atop the best-fitting debris model of Law & Majewski (2010a). The colors in the figure were chosen to match those used by Law & Majewski (2010a), who color-coded points along the stream according to the orbital passage on which they became unbound. Gold points correspond to debris stripped during the two most recent perigalactic passages, and magenta during the previous two passages. This portion of the trailing tail has a well-constrained radial velocity trend, which was measured by Majewski et al. (2004) and Monaco et al. (2007), and was one of the constraints on the Law & Majewski (2010a) models. Sgr model trailing tail debris within $\pm 3.0^\circ$ of the position of each Kapteyn line of sight is shown in the right-hand panels of Figure 15 as small open squares. This illustrates that not only do our measured radial velocities agree quite well with the model, but that the dispersion in each field appears to match the distribution of model points. However, we caution that the velocity dispersions we find (see Table 3) are higher than those derived by Majewski et al. (2004) and Monaco et al. (2007) for the trailing tail. It is unclear whether the dispersion is truly intrinsically higher for Sgr trailing tail MSTO populations we sampled than for the M giants previously studied, or whether our derived dispersions are inflated by the large measurement uncertainties for our RVs, velocity zero-point offsets between the many data sets we have combined, or Milky Way foreground/background contamination in our Sgr candidate samples. While we have endeavored to account for all of these factors, a robust conclusion likely requires high-resolution

¹⁷ Note that we are not suggesting that Sgr has stars 15.8 Gyr old – this isochrone is simply meant as a guide to show that these stars could plausibly be BHB stars associated with Sgr. A blue horizontal branch is only seen in the oldest ($\log(\text{age}) > 10.15$) of the Girardi et al. 2004 isochrones at this metallicity.

spectra of trailing-tail MSTO stars.

3.3. Proper Motions

With the sample of Sgr debris candidates identified in each field, we used a maximum-likelihood method to estimate the Sgr absolute proper motions in both spatial directions ($\mu_\alpha \cos(\delta)$, μ_δ). These results are seen in Table 3 with their uncertainties, which include the uncertainty in the proper motion zero point in each field added in quadrature to the maximum likelihood error estimate. The uncertainties for each field depend on many factors, including the depth and quality of the plates, the number of available reference objects (i.e., background QSOs and galaxies) used to convert from relative to absolute proper motions, the number and depth of spectroscopic targets obtained (and thus the number of Sgr candidates identified), and the position of each field relative to the highest-density regions of the stream (i.e., the number of Sgr candidates expected in each field).

Mean proper motions along Galactic coordinates (i.e., $\mu_l \cos b$, μ_b) in each field are compared to the model of Law & Majewski (2010a) as a function of Λ_\odot in the middle and lower panels of Figure 15, with points once again color-coded by the orbital passage in which they became unbound, and model points within $\pm 3.0^\circ$ of each SA line of sight highlighted for guidance. The results for SAs 94, 93, and 117 agree nicely with the model predictions within the uncertainties in μ_b , but show a $\sim 1 - 2\sigma$ offset from the main trend in $\mu_l \cos(b)$ (left middle panel). The mean proper motions along both directions for SA 71 (the leftmost data points in Figure 15) are slightly shifted (by $\sim 1 - 1.5\sigma$) from the mean of the model prediction for this field. A number of factors contribute to the difficulty in selecting a "pure" sample of Sgr debris in SA 71, and there is thus an additional uncertainty (besides the formal errors) in the mean Sgr debris proper motions in this field. First, this field is at somewhat low latitude ($b = -34.7^\circ$), and thus suffers greater contamination from Galactic populations, as evidenced by the extended tail of low-velocity stars in the lower panel of Figure 5. This lower latitude also means that SA 71 suffers significantly more reddening than higher-latitude fields – nearly 0.6 magnitudes of extinction using the Schlegel et al. (1998) maps. Secondly, the distance of Sgr debris increases with Λ_\odot along the portion of the trailing tail in this study, so that stream members in SA 71 are nearly 40 kpc away, making them fainter than in the other fields. Finally, the poor-quality photographic photometry we are limited to in this field renders inscrutable the typical CMD features such as the blue edge of the Galactic disk MSTO and the Sgr upper main sequence.

Assuming distances to Sgr debris in each field as given in Table 3 and values of $V_{\text{circ}} = 220 \text{ km s}^{-1}$ and $R_0 = 8.0 \text{ kpc}$, we converted the measured Sgr debris motions to Galactocentric UVW_{GC} velocities (i.e., Cartesian velocities such that the Sun is moving at 9.0, 232.0, 7.0 km s^{-1} assuming $V_{\text{circ}} = 220 \text{ km s}^{-1}$ and $(U_0, V_0, W_0) = (9.0, 12.0, 7.0) \text{ km s}^{-1}$ (Mihalas & Binney 1981) for the solar motion relative to the Local Standard of Rest; to facilitate direct comparison, values used for these constants are the same as those in the LM10 model), which are shown in Table 3 (note that we placed SAs 92 and 116 – the two fields with no securely identified Sgr members – in a separate section in Table 3. These data are given for completeness, but are not used for subsequent analysis.). The U_{GC} component should dominate the total space velocity of Sgr debris in each of these trailing arm fields. This

can be surmised from Figure 2, which shows that the motion of the Sgr trailing tail is oriented almost parallel to the Galactic X -axis in the $X_{\text{GC}} - Z_{\text{GC}}$ plane. This, in addition to the fact that the Sagittarius orbital plane is only slightly misaligned with the Galactic $X_{\text{GC}} - Z_{\text{GC}}$ plane (Majewski et al. 2003, 2006), suggests that most of the motion in this part of the trailing tail is inward toward the Galactic center and roughly parallel to the Galactic disk (i.e., the $X_{\text{GC}} - Y_{\text{GC}}$ plane) at a distance of ~ 20 -25 kpc below the disk. This is borne out by the measured UVW_{GC} velocities in our SA fields – the U_{GC} component in the four fields with quality measurements is by far the largest component of the 3-D motion. This can be seen even more clearly by considering the proper motions along Galactic coordinates, but in a Galactic rest frame (designated as $\mu'_l \cos(b)$ and μ'_b). These proper motions, given in Table 4, show $\mu'_l \cos(b)$ proper motions of nearly zero in each field – as expected for streaming motions confined to the $X_{\text{GC}} - Z_{\text{GC}}$ -plane. As we will show in Section 4, the offset of these derived longitudinal proper motions (reflected in the V_{GC} Galactic velocity component) from zero can be used to reevaluate the velocity of the Local Standard of Rest (under the assumption that the longitudinal motions *should be* zero).

4. CONSTRAINTS ON MILKY WAY STRUCTURE

As discussed in Section 1.1, the opportune orientation of the Sgr trailing tidal tail means that the observed motion of tidal stream stars in the Galactic Y direction (i.e., towards $[l, b] = [90^\circ, 0^\circ]$) is dominated by the solar reflex motion, which consists of the solar peculiar motion and the Galactic rotational motion at the solar circle (i.e., the Local Standard of Rest Θ_{LSR}). As shown by Majewski et al. (2006), the intrinsic motion of Sgr debris along the Y direction (V_{GC} , contained primarily in the $\mu_l \cos(b)$ component of proper motion) varies only slowly across the region of the trailing tail between $70^\circ \leq \Lambda_\odot \leq 130^\circ$, making the fields of view in which we have deep proper motion data ideal for constraining Θ_{LSR} . It can be seen in Table 3 that V_{GC} for Sgr debris in each of the four fields (SAs 71, 94, 93, and 117) with reliable data is non-zero at the $\sim 1\sigma$ level. Setting aside SA 71, in which it is difficult to securely identify Sgr debris, the remaining three fields exhibit V_{GC} systematically offset to negative values. If indeed the expected V_{GC} for Sgr debris in these fields is zero, this suggests that the value of Θ_{LSR} that was subtracted from the V -component of these velocities was *lower* than it should be – i.e., Θ_{LSR} should be greater than the canonical 220 km s^{-1} .

In this section, we use variations on the LM10 numerical model of the Sgr tidal stream to isolate the contribution to $\mu_l \cos(b)$ from the solar reflex motion and identify the value of Θ_{LSR} favored by our proper motion data.

4.1. N -body models

Though the measured Galactic Cartesian V -velocity (i.e., motion along the Galactic Y -component) of Sgr trailing tidal debris is dominated by Solar reflex motion, there is some contribution of intrinsic Sgr motion to the V -component of debris velocities. In particular, we must consider the following effects when trying to back out Θ_{LSR} from measured V_{GC} for Sgr debris: (1) the slight inclination of the Sgr debris plane to the Galactic XZ_{GC} plane means a small fraction of Sgr space motion is projected onto the measured motions (i.e., the V velocity is in fact a function of both Θ_{LSR} and intrinsic Sgr motion); (2) the Galactic Standard of Rest (GSR) frame radial velocities used to constrain the Sgr model were derived

Table 3
Sagittarius Stream Kinematics in Kapteyn Selected Areas

SA	N	V_{helio} km s ⁻¹	V_{GSR} km s ⁻¹	σ_0 km s ⁻¹	$\mu_\alpha \cos(\delta)$ mas yr ⁻¹	μ_δ mas yr ⁻¹	$\mu_l \cos(b)$ mas yr ⁻¹	μ_b mas yr ⁻¹	U_{GC} km s ⁻¹	V_{GC} km s ⁻¹	W_{GC} km s ⁻¹	distance kpc
71	33	-172.9 \pm 4.9	-141.4 \pm 4.9	25.6 \pm 3.5	0.39 \pm 0.44	-0.55 \pm 0.42	0.66 \pm 0.43	-0.17 \pm 0.43	138.1 \pm 47.1	80.7 \pm 77.1	80.1 \pm 63.3	38.0 \pm 4.5
94	64	-142.4 \pm 2.3	-141.3 \pm 2.3	17.4 \pm 1.8	0.35 \pm 0.27	-2.32 \pm 0.29	1.88 \pm 0.28	-1.40 \pm 0.28	227.9 \pm 34.1	-49.5 \pm 54.0	-12.6 \pm 30.8	29.5 \pm 4.0
93	15	-157.2 \pm 4.7	-114.1 \pm 4.7	16.1 \pm 3.3	0.42 \pm 0.73	-2.66 \pm 0.56	1.60 \pm 0.70	-2.16 \pm 0.60	210.6 \pm 81.3	-101.6 \pm 88.4	-10.7 \pm 45.4	28.0 \pm 3.0
117	43	-90.0 \pm 3.9	-69.3 \pm 3.9	24.0 \pm 2.8	0.02 \pm 0.64	-3.11 \pm 0.72	1.28 \pm 0.65	-2.84 \pm 0.71	229.3 \pm 83.7	-76.8 \pm 94.6	11.5 \pm 24.9	25.0 \pm 4.0
92	6	-158.9 \pm 6.3	-78.4 \pm 6.3	10.6 \pm 8.7	1.34 \pm 1.07	-3.84 \pm 0.66	1.46 \pm 1.06	-3.80 \pm 0.66	145.6 \pm 123.3	-296.9 \pm 107.9	-84.6 \pm 45.6	27.5 \pm 2.5
116	10	-75.4 \pm 6.7	-22.3 \pm 6.7	20.3 \pm 4.9	1.12 \pm 1.04	-3.30 \pm 1.15	-0.67 \pm 1.07	-3.42 \pm 1.12	87.3 \pm 124.3	-170.8 \pm 129.6	-22.7 \pm 35.3	24.5 \pm 2.0

Note. — All calculations assume $V_{\text{circ}} = 220$ km s⁻¹ at $R_0 = 8.0$ kpc. We used the solar peculiar motion of Mihalas & Binney (1981): $(U_0, V_0, W_0) = (9.0, 12.0, 7.0)$ km s⁻¹ (in a right-handed frame).

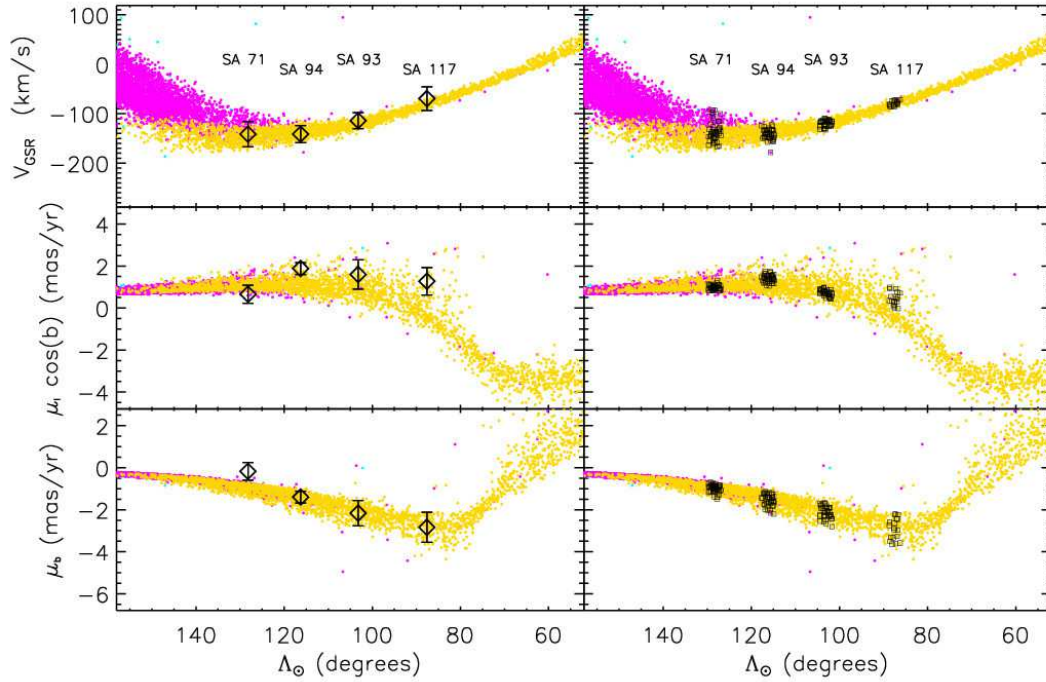


Figure 15. Kinematics of Sgr candidate stars measured in four SA fields (SAs 71, 94, 93, and 117, from left to right) as a function of longitude in the Sgr coordinate system defined by Majewski et al. (2003). From top to bottom, the panels depict GSR-frame radial velocity (V_{GSR}), proper motion along Galactic longitude ($\mu_l \cos b$), and proper motion along latitude (μ_b). Colored points depict trailing tail debris from the best-fit Sagittarius model of Law & Majewski (2010a), with different colors representing debris stripped on successive orbits, as in Law & Majewski (2010a). In each row, the right-hand panels depict stars selected from the model to be within $\pm 3^\circ$ of each of the SA fields as small black squares; these are the points to which we compare the measured kinematics in each field. In the left panels, large open diamonds with error bars represent the maximum likelihood estimates of the mean kinematics of Sgr debris. Note that it is important to compare measured kinematics (on the left) to the “clouds” of small black squares in corresponding fields in the right panels, rather than comparing to the trend defined by all of the colored points. This is necessary because at a given Λ_\odot , the model debris plotted here can come from a large area on the sky. We are interested in comparing only what the model predicts “should be” seen in each pencil-beam field of view, and thus we select only model debris in corresponding regions of the sky. The measured V_{GSR} for Sgr debris matches the model very well in all four fields, and the μ_b proper motions agree in three of the four fields (see the text for discussion of the difficulties in selecting Sgr debris in SA 71, the $\sim 1\sigma$ discrepant point furthest to the left). In $\mu_l \cos b$, however, the measurements for all but one field (again, SA 71) are systematically offset to higher proper motions than predicted by the model. We show that this offset can be accounted for by an upward revision of Θ_{LSR} , the rotation speed at the Solar circle.

assuming a value of Θ_{LSR} ; (3) changing Θ_{LSR} correspondingly changes the Milky Way mass scale, which thus affects the space velocity of the Sgr dSph in the models. Therefore, taking into account these dependencies on the assumed value of Θ_{LSR} , we repeat the LM10 analysis, changing Θ_{LSR} to construct self-consistent models for the Sgr tidal stream in each of four choices for the Local Standard of Rest speed, namely $\Theta_{\text{LSR}} = 190, 250, 280, 310$ km s⁻¹ (in addition to the original LM10 value of $\Theta_{\text{LSR}} = 220$ km s⁻¹ used in earlier sections of this paper).

Our methodology is described in detail by LM10. In brief, we constrain the model Sgr dwarf to lie at the observed location $(l, b) = (5.6^\circ, -14.2^\circ)$, distance $D_{\text{Sgr}} = 28$ kpc (Siegel et al. 2011, Siegel et al. 2007), and radial velocity $v_{\text{Sgr}} = 142.1$ km s⁻¹ in the heliocentric frame. The orbital plane is constrained to be that defined by the trailing arm tidal debris, which has experienced minimal angular precession (Johnston et al. 2005), and the speed of Sgr tangential to the line of sight (v_{tan} ; see Section 3.3 of LM10) is constrained by a χ^2 minimization fit to the radial velocities of trailing arm tidal debris. We fix

Table 4

Galactic Frame-of-Rest Proper Motions of Sagittarius Debris in Selected Areas

SA	V_{GSR} (km s ⁻¹)	$\mu'_\alpha \cos(\delta)$ (mas yr ⁻¹)	μ'_δ (mas yr ⁻¹)	$\mu'_l \cos(b)$ (mas yr ⁻¹)	μ'_b (mas yr ⁻¹)
71	-141.4	-0.47	0.39	-0.61	0.00
94	-141.3	-0.77	-1.09	0.22	-1.31
93	-114.1	-0.71	-1.36	0.00	-1.54
117	-69.3	-1.17	-1.57	-0.44	-1.91

^aAll calculations assume $V_{\text{circ}} = 220 \text{ km s}^{-1}$ at $R_0 = 8.0 \text{ kpc}$, and solar peculiar motion of $(U_0, V_0, W_0) = (9.0, 12.0, 7.0) \text{ km s}^{-1}$ (in a right-handed frame).

Table 5

Masses of Galactic Bulge and Disk Components in the Sagittarius Models

Θ_{LSR} (km s ⁻¹)	M_{disk} (M_\odot)	M_{bulge} (M_\odot)	α -
190	6.8×10^{10}	2.3×10^{10}	0.68
220	1.0×10^{11}	3.4×10^{10}	1.00
250	1.4×10^{11}	4.6×10^{10}	1.35
280	1.8×10^{11}	6.0×10^{10}	1.76
310	2.2×10^{11}	7.5×10^{10}	2.21
264	1.5×10^{11}	5.2×10^{10}	1.53
232	1.1×10^{11}	3.9×10^{10}	1.14

^aThe mass of the disk and bulge components in each of the models of the Sgr stream. Each model is specified by the value of Θ_{LSR} that constrained the fit; the 220 km s^{-1} model is that of LM10. The ratio of disk to bulge mass is constant throughout – the constant α is the scaling factor, such that $M_{\text{disk}} = \alpha * M_{\text{disk}, 220 \text{ km/s}}$ and $M_{\text{bulge}} = \alpha * M_{\text{bulge}, 220 \text{ km/s}}$. The total mass, axis ratios, and scale length of the Galactic dark matter halo were fixed to the best-fit values of LM10.

the mass and radial scalelength of the Sgr progenitor so that the fractional mass loss history of the dwarf is similar in all models to that of LM10.

The adopted Milky Way Galactic mass model consists of three components: a Hernquist spheroid (representing the Galactic bulge), a Miyamoto & Nagai (1975) disk, and a logarithmic dark matter halo. The Local Standard of Rest in this model is given by:

$$\Theta_{\text{LSR}} = \sqrt{R_\odot (a_{\text{bulge}} + a_{\text{disk}} + a_{\text{halo}})} \quad (1)$$

where a_{bulge} , a_{disk} , and a_{halo} respectively represent the gravitational acceleration exerted on a unit-mass at the location of the Sun due to the Galactic bulge, disk, and halo components. In the LM10 model (for which $\Theta_{\text{LSR}} = 220 \text{ km s}^{-1}$), the bulge/disk/halo respectively contribute 32%/49%/19% of the total centripetal acceleration at the position of the Sun, corresponding to bulge/disk masses $M_{\text{bulge}} = 3.4 \times 10^{10} M_\odot$ and $M_{\text{disk}} = 1.0 \times 10^{11} M_\odot$, and a total mass within 50 kpc of $4.5 \times 10^{11} M_\odot$.

Since the baryonic Galactic disk and bulge components are the dominant factors in determining Θ_{LSR} (together comprising $> 80\%$ of the total centripetal force), we therefore scale the total bulge + disk mass as necessary to normalize the rotation curve at the solar circle ($R_\odot = 8 \text{ kpc}$) to the chosen value of Θ_{LSR} . The masses of the disk and bulge components in each of the models are given in Table 5. We leave the *ra-*

tio of bulge/disk mass fixed in order to preserve the shape of the rotation curve interior to the solar circle. In addition, we fix the Galactic dark matter halo parameters (mass, axis ratios, and scalelength) to the best-fit values derived by LM10 since these authors found that these values were relatively insensitive to factors of ~ 2 variation in the mass scale of the baryonic Galactic components.

4.2. Results

Constraints on Θ_{LSR} were derived in two ways. In the first of these methods, we assumed (as argued previously in this paper, as well as in MLPP) that the dominant contribution to the measured $\mu_l \cos(b)$ component of Sgr motion is due to the solar rotation, and that the largest component of Θ_{LSR} is along $\mu_l \cos(b)$. We have shown that these are reasonable first-order assumptions, and thus use only the longitudinal proper motions as constraints on fitting Θ_{LSR} in our first attempt. After doing so, however, we performed a similar analysis, but using all three dimensions of Sgr debris motions as constraints to determine Θ_{LSR} . In the following, we present both results, which come out somewhat different from each other (though consistent within 1σ). Fits using only $\mu_l \cos(b)$ tend to prefer relatively high values of Θ_{LSR} , while those constrained by full 3-D kinematics tend toward lower values more in line with the IAU standard of 220 km s^{-1} .

4.2.1. Θ_{LSR} Constraints Using Only $\mu_l \cos(b)$ Motions of Sgr Debris

We quantify the agreement of our proper motions with those of simulated Sgr tidal debris from each of our grid of models using a χ^2 statistic. The χ^2 fitting was performed using mean Sgr debris proper motions in only SAs 71, 94, 93, and 117 – as discussed in Section 3.1, the results in SAs 92 and 116 are unreliable for a variety of reasons. For our model comparison, we first select all LM10 Sgr model points within $\pm 3.0^\circ$ in both Λ_\odot and (α, δ) of each SA field. The large area (relative to the $40' \times 40'$ coverage of each SA field) used to select model debris corresponding to each SA position ensures that enough N -body particles are selected for robust measurement of model debris motions at each position. This also makes the fitting less sensitive to small-scale differences in positions and densities of debris stars between the models and the actual stream that arise due to the vagaries of the modeling and our incomplete knowledge of the Sgr trailing tail properties. Figure 16 shows the model debris $\mu_l \cos(b)$ as a function of Λ_\odot for each of the five Sgr simulations, with points corresponding to each SA field shown as small open gray squares. It is clear that $\mu_l \cos(b)$ changes very little over the 6° ranges in (α, δ) used. Furthermore, the small number of selected model points, even in such a large selection region, shows that these broad selection criteria are necessary to have sufficient model points for comparison. The maximum likelihood proper motion results in SAs 71, 94, 93, and 117 are shown in Figure 16 as open black diamonds, with error bars reflecting 1σ uncertainties. It can be seen in the figure that the models with $\Theta_{\text{LSR}} > 220 \text{ km s}^{-1}$ tend to reproduce the longitudinal proper motions for most of the fields better than the standard 220 km s^{-1} value of this fundamental constant. Note that SA 71, at $\Lambda_\odot = 128^\circ$, is the exception to this trend – as discussed in Section 3.3, identifying bona fide Sgr debris in this field is more difficult than the others and so these data are more suspect.

Each of the Sgr model simulations provides predicted kinematics of Sgr debris for a Galactic potential constrained by a

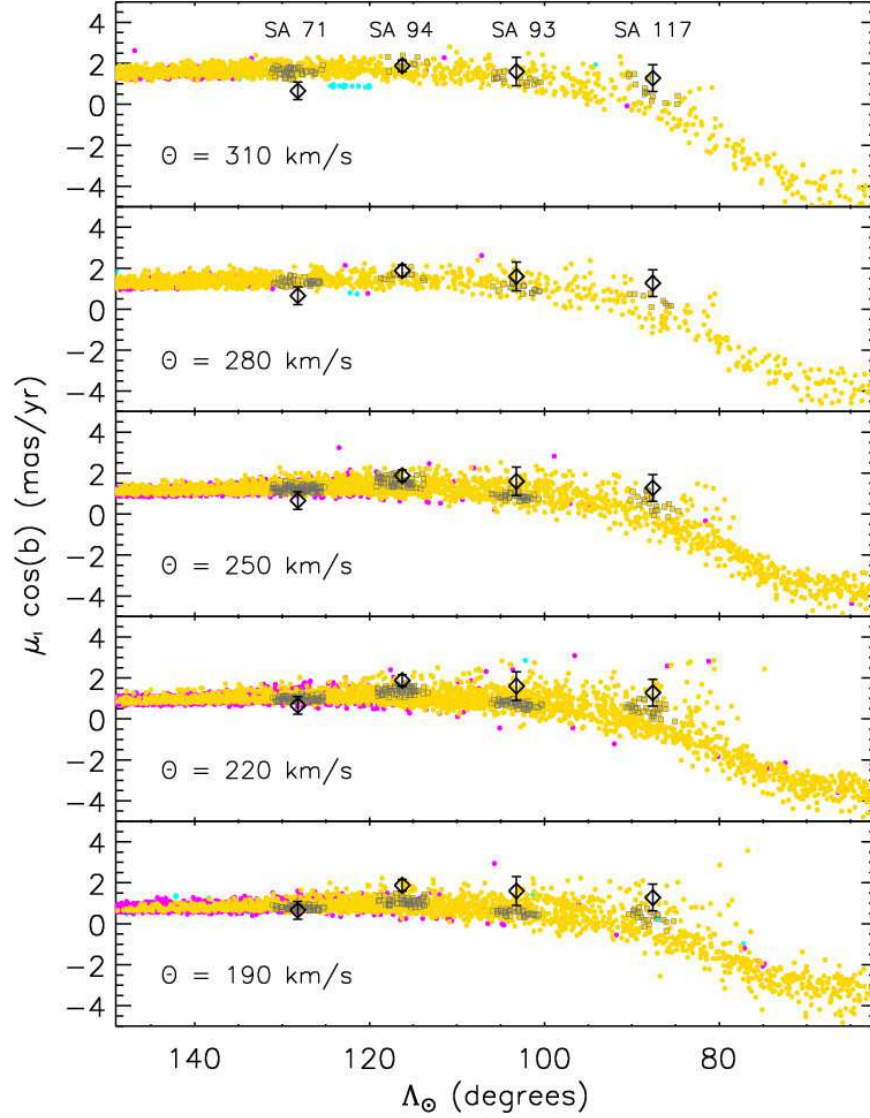


Figure 16. Mean longitudinal proper motions, $\mu_l \cos(b)$ (large open diamonds with error bars), in (from left to right) SAs 71, 94, 93, and 117 as a function of Λ_\odot . Model debris from the Sgr simulations are shown as the colored points; from top to bottom, these represent models with $\Theta_{\text{LSR}} = 310, 280, 250, 220$, and 190 km s^{-1} . The sudden drop in $\mu_l \cos(b)$ for $\Lambda_\odot \lesssim 90^\circ$ is due to the inversion in sign that occurs as the debris sweeps past the South Galactic pole. Small open gray squares denote the model debris corresponding (within $\pm 3^\circ$ in RA, Dec, and Λ_\odot) to each SA field. It is clear that higher values of Θ_{LSR} provide a better match of the small gray squares to the observed $\mu_l \cos(b)$ values in the Selected Areas (diamonds).

given value of Θ_{LSR} . As discussed previously, the Galactic V -component of the Sgr debris space velocity along the trailing tail contains little contribution due to the Sgr motion; nearly all the V velocity (as measured by the $\mu_l \cos(b)$ component of the proper motion) is reflected Solar motion. Thus, to first order, we can simply compare our mean Sgr proper motions along Galactic longitude in the trailing tidal tail to our models of Sgr debris for different values of Θ_{LSR} and determine the value of Θ_{LSR} that best reproduces the measured PMs. To do so, we defined a χ^2 residual:

$$\chi_\mu^2 = \sum_i \frac{(\mu_{l,\text{SA}}[i] - \mu_{l,\text{mod}}[i])^2}{\sigma_{\mu_{l,\text{SA}}[i]}} \quad (2)$$

where $\mu_{l,\text{SA}}[i]$ represents the mean $\mu_l \cos(b)$ proper motion in each of the four SA fields, and $\mu_{l,\text{mod}}[i]$ the mean proper motion of the corresponding model debris for each field.

The residuals are weighted by the uncertainty, $\sigma_{\mu_{l,\text{SA}}[i]}$, in each SA proper motion. This χ^2 statistic was initially calculated for the proper motions presented in Table 3 relative to each of the five Sgr debris models (corresponding to $\Theta_{\text{LSR}} = 190, 220, 250, 280, 310 \text{ km s}^{-1}$). Rather than running new (and laborious) N -body simulations for many intermediate values of Θ_{LSR} and calculating χ^2 for each of them, we choose to find the minimum χ^2 by fitting a parabola to the χ^2 results for each of the five modeled values of Θ_{LSR} . The results of the χ^2 calculation and the parabolic fit are seen in Figure 17 for the proper motions of the “best” SA samples given in Table 3. The minimum of the parabola yields $\Theta_{\text{LSR,min}} = 270.4 \text{ km s}^{-1}$.

To estimate the uncertainty in Θ_{LSR} , we choose a bootstrap (resampling with replacement) method (see Andrae 2010 and references therein). This technique uses the entire sample of

individual Sgr candidate star proper motions, and thus yields an estimate of the errors in Θ_{LSR} including the effects of proper motion measurement errors and "contamination" of the proper-motion samples by Milky Way stars. Our selected samples of Sgr candidates in SAs 71, 94, 93, and 117 should contain mostly Sgr debris, plus some amount of contamination by MW stars that will vary depending on the depth of the proper-motion and radial-velocity catalogs, the local Sgr stream density, and the Galactic latitude of each field. From the Sgr samples in each field, we performed 100,000 bootstrap resamplings, wherein N random selections were made from the N original stars in each field (i.e., the catalogs of candidates were resampled with replacement). Iteratively 3σ -clipped mean proper motions of these resampled Sgr candidates were measured, and the mean proper motions used in an identical χ^2 fitting routine to that described above. Assuming that the contaminants in each sample are somewhat uniformly distributed in their kinematical quantities, this method should yield a statistically robust result for Θ_{LSR} and its uncertainty (due to both the intrinsic measurement errors and the MW contamination). The best-fitting values of Θ_{LSR} for these 100,000 samples are given as a histogram in the left panel of Figure 18, along with a Gaussian fit (red curve) to the results. From this Gaussian, we derive a final value of $\Theta_{\text{LSR}} = 264 \pm 23 \text{ km s}^{-1}$.

4.2.2. Θ_{LSR} Constraints Using Three-Dimensional Motions of Sgr Debris

The constraints we derived on Θ_{LSR} using only the longitudinal proper motions assume that the contributions of Θ_{LSR} to μ_b and V_{GSR} are negligible. If the Sgr orbital plane was exactly coincident with the Galactic XZ_{GC} plane, then indeed the rotation velocity at the solar circle would only be reflected in the $\mu_l \cos(b)$ motions. In reality, the Sgr orbital plane is *not* perfectly aligned with the Milky Way XZ -plane, so there is some projection of V_{circ} onto μ_b and V_{GSR} . In fact, for Sgr debris in the four fields of view comprising this study (SAs 71, 94, 93, and 117), only (75%, 87%, 61%, 58%, respectively) of the total value of Θ_{LSR} is projected onto $\mu_l \cos(b)$. We ran the χ^2 fitting again, but this time including all three dimensions of the motion as constraints. The bootstrap analysis gave a result of $\Theta_{\text{LSR}} = 232 \pm 14 \text{ km s}^{-1}$ – a histogram of the bootstrap results is seen in the right panel of Figure 18. This mean value is lower by $\sim 1.4\sigma$ than the result using only $\mu_l \cos(b)$. Formally, this is a better fit than the one-dimensional result (with uncertainty of 14 km s^{-1} compared to an uncertainty of 23 km s^{-1} from the fits using only longitudinal proper motions), but the two are consistent within their 1σ uncertainties.

Finally, we performed the same exercise using all three dimensions of Sgr debris motions, but excluding the less reliable SA 71 field. The uncertain identification of Sgr debris in SA 71 is likely the reason this field (at $\Lambda_{\odot} = 128^\circ$) is an outlier from the predicted kinematical trends in Figures 15 and 16. The bootstrap fit using only SAs 94, 93, and 117 yields $\Theta_{\text{LSR}} = 244 \pm 17 \text{ km s}^{-1}$. This slightly higher value for Θ_{LSR} suggests that (as is evident in Figures 15 and 16) the Sgr candidates in SA 71 skew our results toward lower Θ_{LSR} .

Ultimately, we have derived three estimates of Θ_{LSR} – one based on a simple one-dimensional analysis (using all four fields) that gave $264 \pm 23 \text{ km s}^{-1}$, another based on three-dimensional data yielding $232 \pm 14 \text{ km s}^{-1}$, and a final 3-D result with SA 71 excluded, which gave $244 \pm 17 \text{ km s}^{-1}$. It is likely that the true result is somewhere between the two

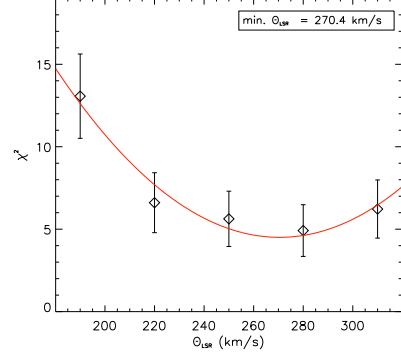


Figure 17. Total χ^2 residuals for the final mean proper motions relative to corresponding model debris. Each point represents a χ^2 for one of the five models in which we vary Θ_{LSR} from 190–310 km s^{-1} . A parabola fit to the results (the red curve) yields a minimum χ^2 at $\Theta_{\text{LSR}} = 270.4 \text{ km s}^{-1}$.

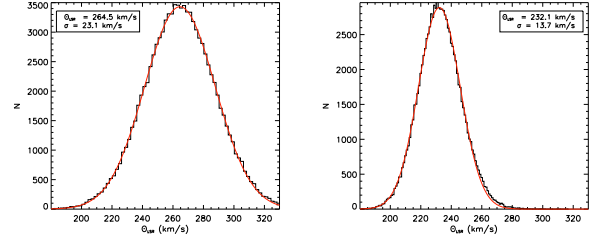


Figure 18. Resulting Θ_{LSR} corresponding to the minimum χ^2 of 100,000 bootstrap resamplings of the individual stellar proper motions in each SA field. The left panel shows fits using only the $\mu_l \cos(b)$ component of Sgr debris motions in SAs 71, 94, 93, and 117. A Gaussian fit (overlaid as the red curve) to the results yields $\Theta_{\text{LSR}} = 264 \pm 23 \text{ km s}^{-1}$. The right panel shows the results using all three dimensions of Sgr debris motions (i.e., $\mu_l \cos(b)$, μ_b , and V_{GSR}) as constraints, which yields $\Theta_{\text{LSR}} = 232 \pm 14 \text{ km s}^{-1}$.

extremes (264 km s^{-1} and 232 km s^{-1}) from our methods.

4.2.3. Sgr Disruption Models For Best-Fitting Θ_{LSR}

We now repeat the N -body analysis described in Section 4.1 two times, first taking $\Theta_{\text{LSR}} = 264 \text{ km s}^{-1}$ as a constraint on the models, then again using $\Theta_{\text{LSR}} = 232 \text{ km s}^{-1}$. The resulting N -body model for the 264 km s^{-1} case matches the angular position, distance, and radial velocity trends of the observed Sgr tidal streams (using all of the observational constraints included in the original LM10 model) almost equally as well as did the LM10 model (formally, $\chi = 3.1$ for the $\Theta_{\text{LSR}} = 264 \text{ km s}^{-1}$ model, compared to $\chi = 3.4$ for the LM10 model; see discussion in Section 4.3 of LM10). In addition, as demonstrated in the left panel of Figure 19 the proper motion of the remnant core of the Sgr dwarf in this revised model ($\mu_l \cos(b) = -2.54 \text{ mas yr}^{-1}$, $\mu_b = 1.92 \text{ mas yr}^{-1}$) is a substantially better match to observations (e.g., Dinescu et al. 2005; Pryor et al. 2010) than was the LM10 model.

However, the N -body model in a Milky Way halo with $\Theta_{\text{LSR}} = 232 \text{ km s}^{-1}$ fits equally well as does the 264 km s^{-1} case, $\chi = 3.1$. For this model, the Sgr core proper motion (seen in the right panel of Figure 19) is intermediate between those of the LM10 model and the 264 km s^{-1} result, as might be expected. In this case, the proper motions are discrepant with both the Dinescu et al. (2005) and Pryor et al. (2010) results at the $\sim 1.5\sigma$ level. In the following subsection we discuss the ramifications of these Θ_{LSR} results for the Milky Way halo.

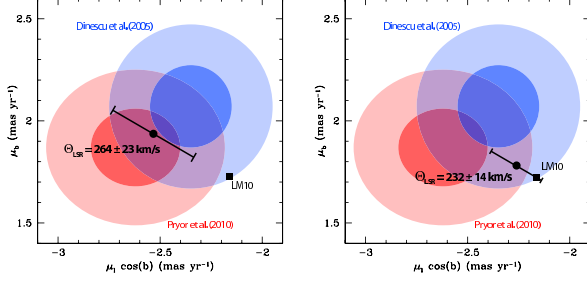


Figure 19. Proper motion estimates for the Sgr core in Galactic coordinates. Blue and red shaded ellipses show 1σ and 2σ uncertainty regions around the measurements of Dinescu et al. (2005) and Pryor et al. (2010) respectively. The proper motion of the Sgr model dwarf described by LM10 ($\Theta_{\text{LSR}} = 220 \text{ km s}^{-1}$) is indicated by a filled black square. In the left panel the 1σ range of proper motions corresponding to the value $\Theta_{\text{LSR}} = 264 \pm 23 \text{ km s}^{-1}$ we found using only the $\mu_l \cos(b)$ component of Sgr debris motions is indicated by the error bars surrounding the filled black circle. The right panel is similar, but for the result ($\Theta_{\text{LSR}} = 232 \pm 14 \text{ km s}^{-1}$) using all three dimensions of Sgr debris kinematics. The orientation of the error bars represents the direction to which changes in Θ_{LSR} correspond in this diagram; the proper motion of the Sgr core is constrained to lie along this line because the orbital plane is fixed by the observed position of the tidal debris leading and trailing Sgr, which trace its orbit.

4.3. Robustness of the Galactic Mass Models

The results for Θ_{LSR} from our analysis in the previous subsection suggest that the true value of Θ_{LSR} as constrained by Sgr trailing tail debris likely lies between 232–264 km s^{-1} , but that more (or more sensitive) proper motion measurements of Sgr trailing debris are needed to resolve this issue. In this subsection, we will discuss the implications of the Θ_{LSR} constraints resulting from our two methods; we remind the reader that the upper end of the range (i.e., the 264 km s^{-1} result) is less robustly determined than the results that produced lower values of the circular velocity. However, we include this value in our discussion to present the reader with the range of possible ramifications of what, in either case, represents an upward revision of Θ_{LSR} from the accepted value.

The value of $\Theta_{\text{LSR}} = 232 \pm 14 \text{ km s}^{-1}$ we found using all three dimensions of Sgr debris kinematics is consistent with the canonical 220 km s^{-1} value at the roughly 1σ level. However, this value is also consistent (within the 1σ uncertainties) with recent determinations of Θ_{LSR} that have found the rotation speed to be higher than the standard 220 km s^{-1} value [e.g., Reid et al. (2009) – $\Theta_{\text{LSR}} = (254 \pm 16)(R_0/8.4) \text{ km s}^{-1}$; Bovy et al. (2009) – $\Theta_{\text{LSR}} = 244 \pm 13 \text{ km s}^{-1}$]. For a change in Θ_{LSR} of only about 10 km s^{-1} , it is difficult to make any conclusions about whether the additional mass required to increase the rotation speed must reside in the Galactic halo or the disk/bulge. We note that placing the additional mass in the disk and bulge (with the halo fixed) yields $M_{\text{bulge}} = 3.9 \times 10^{10} M_{\odot}$ and $M_{\text{disk}} = 1.1 \times 10^{11} M_{\odot}$ for the 232 km s^{-1} model – an increase of $\sim 10\%$ over the disk and bulge mass from the model of LM10. The relatively high value of $\Theta_{\text{LSR}} = 264 \pm 23 \text{ km s}^{-1}$ found by our analysis using only the $\mu_l \cos(b)$ motions would require that the mass of the Galactic bulge and disk components be increased by $\sim 50\%$ from the values assumed by LM10 to $M_{\text{bulge}} = 5.2 \times 10^{10} M_{\odot}$ and $M_{\text{disk}} = 1.53 \times 10^{11} M_{\odot}$. This disk mass is near the peak of the probability distribution ($M_{\text{disk}} = 1.35 \times 10^{11} M_{\odot}$) found by Koposov et al. (2010) based on fitting the GD-1 stream in a three-component gravitational potential similar to our own. We caution however that the orbit of Sgr is largely insensitive to the *distribution* of the excess mass between the two

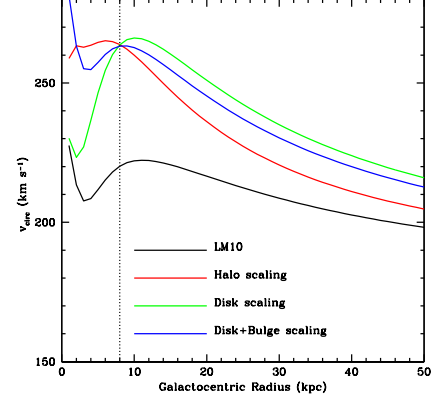


Figure 20. Model Milky Way rotation curves as a function of radius from the Galactic center. Solid blue/green/red lines respectively represent rotation curves with $\Theta_{\text{LSR}} = 264 \text{ km s}^{-1}$ achieved via scaling the Galactic bulge+disk, Galactic disk alone, and Galactic halo alone. Included for comparison is the rotation curve of the original LM10 model (solid black line) normalized to $\Theta_{\text{LSR}} = 220 \text{ km s}^{-1}$. The vertical dotted line represents the location of the Sun at $R_{\odot} = 8 \text{ kpc}$.

baryonic components, and solutions that yield similar χ^2 can be found by ascribing all or part of the needed adjustment in Θ_{LSR} to changes in the mass of either the disk or bulge components alone. We do note, however, that the relative fraction of the total disk+bulge mass in each component is constrained by the need to reproduce the shape of the observed Milky Way rotation curve interior to R_{\odot} (see Figure 20).

The total mass of the Milky Way interior to 50 kpc in the 264 km s^{-1} model is $5.2 \times 10^{11} M_{\odot}$, similar to the value of $4.5 \times 10^{11} M_{\odot}$ in the LM10 model. Since we have accounted for the increased $\Theta_{\text{LSR}} = 264 \text{ km s}^{-1}$ by increasing the disk+bulge mass (which is a relatively small component of the total virial mass), the mass of the Milky Way interior to 200 kpc is $M_{\text{vir}} = 1.6 \times 10^{12} M_{\odot}$, similar to the value of $1.5 \times 10^{12} M_{\odot}$ derived by LM10 assuming that $\Theta_{\text{LSR}} = 220 \text{ km s}^{-1}$.

We note that it was not possible to obtain a satisfactory model (within our parameterization of the Milky Way components; exploration of different dark halo models is beyond the scope of this work) for the Sgr stream by leaving both the bulge and disk masses fixed at their LM10 values and accounting for changes in Θ_{LSR} by scaling the dark matter halo. The dark matter halo profile is characterized by the parameters v_{halo} and r_{halo} (see Eqn. 3 of LM10)¹⁸, which describe the total mass normalization and radial scalelength of the halo respectively. Since dark matter in the LM10 model contributes only 19% of the total centripetal acceleration in the solar neighborhood, v_{halo} must be scaled up drastically (by a factor of ~ 3 in total halo mass) to increase Θ_{LSR} from 220 km s^{-1} to 264 km s^{-1} , and necessitates a large increase in the space velocity of Sgr along its orbit (to $\sim 400 \text{ km s}^{-1}$) to produce a leading arm debris stream at an observed peak distance of $\sim 50 \text{ kpc}$ (see Figure 6 of LM10). However, such a rapidly moving satellite model yields radial velocities along the tidal debris streams that are systematically discrepant from observations by $\sim 75 \text{ km s}^{-1}$. Similarly, it is neither possible to obtain a satisfactory fit for larger Θ_{LSR} values ($\Theta_{\text{LSR}} \gtrsim 280 \text{ km s}^{-1}$, for which

¹⁸ The halo triaxiality is an added complication that has little bearing on the present discussion.

the halo mass scaling problem is even more extreme), nor for much lower values ($\Theta_{\text{LSR}} \sim 190 \text{ km s}^{-1}$, because the baryonic bulge+disk mass component alone require $\Theta_{\text{LSR}} > 190 \text{ km s}^{-1}$).

Another possibility we considered was to again fix the baryonic mass (i.e., the bulge+disk component), but to a smaller value than the LM10 model, and allow the halo mass to vary. In particular, we attempted to fit a model with $\Theta_{\text{LSR}} = 232 \text{ km s}^{-1}$, but with the bulge+disk mass decreased by 10% from the LM10 values. Even this small change in the baryonic mass required scaling up the dark matter halo mass by $\sim 50\%$ to keep $\Theta_{\text{LSR}} = 232 \text{ km s}^{-1}$. The best-fit N -body model in this case fit the Sgr trailing-tail velocities, but was a poor fit to the leading arm SDSS distances because of the increased speed of the Sgr core necessitated by the much larger halo. This illustration highlights the large changes in the halo mass effected by even small changes in the baryonic mass or the LSR velocity when fitting to observational data on the Sgr system. In fact, it is a testament to how well-constrained the Sgr system is by the current observational data that we are unable to fit the data if we change the dark halo model substantially.

One possible way to construct an N -body model of the Sgr dwarf that fits the observational data relatively well while dramatically changing Θ_{LSR} is to adopt a Galactic halo whose scalelength is a factor of ~ 10 shorter than commonly adopted (from $r_{\text{halo}} = 12 \text{ kpc}$ in the LM10 model to $r_{\text{halo}} = 1 \text{ kpc}$). However, the Galactic rotation curve implied by such a short halo scalelength declines steeply outside the solar circle (Figure 20), in conflict with observations (e.g., Sofue et al. 2009). We therefore conclude that it is not possible to satisfactorily model the Sgr dwarf in a Milky Way model with the bulge and disk masses fixed at the LM10 values of $M_{\text{bulge}} = 3.4 \times 10^{10} M_{\odot}$, $M_{\text{disk}} = 1.0 \times 10^{11} M_{\odot}$, and the Milky Way halo scaled to produce Θ_{LSR} much higher than 220 km s^{-1} . Thus our (and other recent) suggestions that Θ_{LSR} is due an upward revision implies that the disk and/or bulge components – but *not* the halo – of the Milky Way are more massive than previously thought.

5. ABUNDANCES

While the spectra in the Selected Areas were obtained primarily with kinematics in mind, they have sufficient resolution and, for a large fraction of stars, sufficient S/N , to obtain information not only on metallicity but also abundance patterns. This allows us an independent estimate of abundance distributions that, while of lower precision than the echelle work of Monaco et al. (2005, 2007) and Chou et al. (2007, 2010), is derived for many Sgr stars, and is less biased than those M-giant studies.

5.1. Sgr Metallicity

Metallicities were measured for all stars using a software pipeline entitled "EZ_SPAM" (Easy Stellar Parameters and Metallicities), details of which will appear in a forthcoming paper (Carlin et al. 2011, *in prep.*). EZ_SPAM relies on the well-understood and calibrated Lick spectral indices (see, e.g., Worthey et al. 1994; Friel 1987) to measure stellar properties from low-resolution spectra. In particular, estimates of $[\text{Fe}/\text{H}]$ are derived for target stars using eight Fe indices combined with the $\text{H}\beta$ index. Calibration of these multi-dimensional data comes from fits of known $[\text{Fe}/\text{H}]$ values as a function of the Lick Fe and $\text{H}\beta$ indices for stars in the atlas of Schiavon (2007, based on the spectra of Jones 1998). The

EZ_SPAM code yields $[\text{Fe}/\text{H}]$ measurements with 1σ precision of $\sim 0.3 \text{ dex}$ at $S/N \approx 20$, decreasing to $\sim 0.1 \text{ dex}$ at higher signal-to-noise ($S/N \gtrsim 50$).

Table 6
Mean $[\text{Fe}/\text{H}]$ for Sgr Debris in Kapteyn Selected Areas of This Study

SA	$\langle [\text{Fe}/\text{H}] \rangle$	$\sigma_{[\text{Fe}/\text{H}]}$	$N_{[\text{Fe}/\text{H}]}$ ^a	Λ_{\odot} (degrees)
71	-1.14 ± 0.19	0.97 ± 0.14	24	128.2
94	-1.13 ± 0.08	0.61 ± 0.06	57	116.3
93	-1.25 ± 0.11	0.47 ± 0.08	23	103.2
92	-0.97 ± 0.16	... ^b	2	90.1
117	-1.08 ± 0.08	0.52 ± 0.06	43	87.6
116	-1.21 ± 0.21	0.64 ± 0.15	10	74.9

^aNumber of spectra with $S/N > 20$ providing reliably-measured $[\text{Fe}/\text{H}]$.

^bCannot be measured for this field – too few spectra.

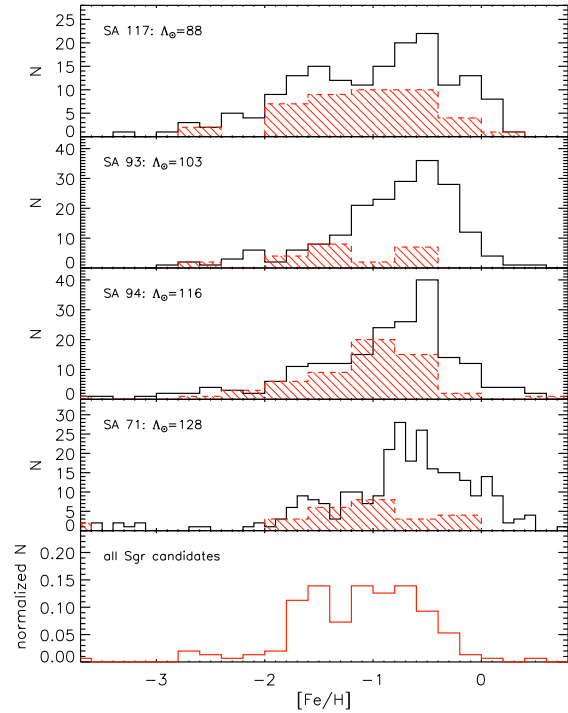


Figure 21. Measured values of $[\text{Fe}/\text{H}]$ for all stars having spectra with $S/N > 20$ in each SA field. The (red) hashed histogram is made up of Sgr candidates from our final samples in each field, and the solid black line represents all other stars (i.e., mostly Milky Way field stars, with perhaps some unidentified Sgr debris included) for which we obtained spectra. The distribution of Sgr metallicities is clearly different from that of the field stars in all of these regions (except perhaps SA 117, which is somewhat ambiguous), peaking at a more metal-poor mean value in each field. The bottom panel shows the metallicity distribution function (MDF) for all four fields in the $88^\circ < \Lambda_{\odot} < 128^\circ$ portion of the trailing tail in our study. This fractional MDF consists of all the Sgr debris metallicities (red histograms) from the previous four panels, normalized by the total number of stars (147) in the sample.

The metallicity distribution for all well-measured stars (i.e., those with spectra having $S/N > 20$) in each of the four fields (SAs 71, 94, 93, and 117) in which Sgr debris are reliably identified is given in Figure 21. For each field, the solid (black) histogram shows $[\text{Fe}/\text{H}]$ of non-Sgr stars, and the

hashed (red) histogram gives the distribution of $[\text{Fe}/\text{H}]$ for stars selected to be Sgr members. The bottom panel represents the distribution of metallicities for all Sgr members from the four trailing-tail fields, normalized by the total number of stars (147) in the sample to produce a fractional distribution. In each field, Sgr members are typically more metal-poor than the field stars, with the possible exception of those in SA 117.

For each SA field in the survey, a maximum likelihood estimate for $[\text{Fe}/\text{H}]$ was derived from all well-measured stars in the final Sgr candidate sample. The resulting values for Sgr debris metallicities in each field are given in Table 6 along with $\sigma_{[\text{Fe}/\text{H}]}$, the dispersion in $[\text{Fe}/\text{H}]$ about the mean. As was the case for the kinematics in SAs 92 and 116, we regard the $[\text{Fe}/\text{H}]$ results in these fields (and, to a lesser degree, those in SA 71) with some skepticism, because the identification of Sgr debris in these fields is rather unreliable. The mean metallicities for Sgr stars are displayed in Figure 22 as a function of Λ_{\odot} ; solid squares depict SAs 71, 94, 93, and 117 (i.e., the “well-measured” fields), with open symbols included for SAs 92 and 116. Error bars represent the uncertainties in the mean value from the maximum likelihood estimator; however, the scatter of $[\text{Fe}/\text{H}]$ for Sgr candidates in each field is rather large. Typical fields have $\sigma_{[\text{Fe}/\text{H}]} = 0.5 - 0.6$ dex about the quoted mean values, similar to the broad metallicity distribution function for Sgr stars seen by, e.g., Smecker-Hane & McWilliam (2002), Zaggia et al. (2004), Siegel et al. (2007), and Monaco et al. (2005). The scatter is even larger in SA 71 (at $\Lambda_{\odot} = 128^{\circ}$); this may arise for a number of reasons. As can be discerned from Figure 1, SA 71 may be sampling Sgr debris stripped on multiple pericentric passages (i.e., both gold and magenta debris may be present in this field). Furthermore, this is the lowest-latitude field among those in this study, and thus may be also suffering more contamination from Galactic thick disk stars. Finally, we note that SA 71 has been shown by Casetti-Dinescu et al. (2008) to contain a significant number of stars from the “Monoceros stream” overdensity, which could contribute to the inflation of the metallicity dispersion in this field, though it is unlikely that many Monoceros stars would lie within our Sgr radial velocity criteria for this field. Also shown in Figure 22 is a solid line at constant $[\text{Fe}/\text{H}] = -1.15$, which is the mean value from the four well-measured fields; the tight correspondence of the mean values of each field to this line is consistent with the notion that debris along this narrow stretch of the trailing tail has constant metallicity. However, there is a hint of a shallow gradient, which we confirm by fitting a linear trend to the four good data points. This fit, overlaid as a dashed line in Figure 22, is $[\text{Fe}/\text{H}] = -0.991 \pm 0.003 - (0.0014 \pm 0.0036) \Lambda_{\odot}$. While suggestive of a slight gradient, the slope given is also consistent with zero within the errors of the fit. This is not surprising considering that nearly all debris in the portion of the stream contained within this study is expected to have been stripped on the same pericentric passage of the Sgr core, as evidenced by the fact that all of our fields overlap gold-colored debris in Figure 1 (i.e., debris that became unbound during the last two perigalactic passages; see Law & Majewski 2010a for more detail about the color scheme used).

Our measured metallicity of $[\text{Fe}/\text{H}] \sim -1.2$ for Sgr trailing debris is ~ 0.6 dex more metal-poor than the result obtained by Keller et al. (2010) for trailing-tail M-giants. This is not surprising, as M giants are biased toward relatively younger, more enriched stellar populations. In spite of this difference between the older, metal-poor Sgr stars in our SA fields and

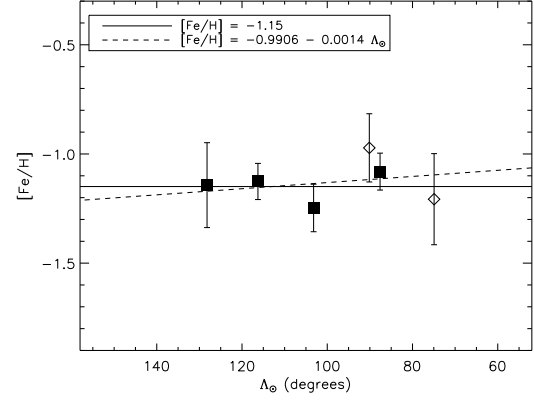


Figure 22. Measured values of $[\text{Fe}/\text{H}]$ for Sgr candidates in each SA field as a function of Sgr longitude, Λ_{\odot} . Filled squares and diamonds (and associated error bars) show the maximum likelihood estimate from the individual Sgr candidates in each field (diamonds are the two fields lacking secure identification of candidates). The mean value of the four well-measured fields (the filled squares), $[\text{Fe}/\text{H}] = -1.15$, is represented by the solid line that reproduces the measurements well. A linear fit to the same four fields is shown as a dashed line, and is suggestive of a slight metallicity gradient of 1.4×10^{-3} dex degree $^{-1}$ along the stream (though the fit is consistent with zero slope within the uncertainties).

the more metal-rich M-giants, we measure a shallow gradient in $[\text{Fe}/\text{H}]$ as a function of Λ_{\odot} , with a slope consistent with the Keller et al. (2010) measurement, and just a simple offset in the zero-point metallicity. A more apt comparison for the mean metallicity of Sgr debris in our SA fields is the work of Sesar et al. (2010), who used SDSS Stripe 82 data to develop a new technique for estimating metallicity from photometric data, which relies on combined information from both RR Lyrae variables and main-sequence stars from the same structure. Because SAs 94, 93, and 92 are within Stripe 82 (and, in fact, we have used those SDSS data in our analysis), the Sesar et al. study probes identical stellar populations from the Sgr trailing tail as our work. This is borne out by the fact that our measured $[\text{Fe}/\text{H}] = -1.15$ is in excellent agreement with the value of $[\text{Fe}/\text{H}] = -1.20 \pm 0.1$ derived by Sesar et al. (2010) for Sgr debris along the same portion of the trailing stream.

5.2. Metallicity Distribution Function

Previous attempts to measure the metallicity distribution function (MDF) of the Sgr stream have suffered from both small number statistics and stellar tracers that have an inherent metallicity bias. For example, Chou et al. (2007) measured the MDF for M giant stars at several points along the Sgr leading stream as well as its core; using these data they attempted to reconstruct the MDF that the Sgr stream progenitor would have had several Gyr ago. However, because M giants only form in metal rich stellar populations, this analysis, while able to show that the mean metallicity of stars varies along the stream, was inadequate to assess the MDF across the full metallicity range of the system. In addition, the analysis was based on a relatively small sample (about 7 dozen stars), nearly half of which are in the core of the Sgr dSph. Monaco et al. (2007) derived abundances of Sgr M giants along the *trailing* tidal tail, from which they derived $\langle [\text{Fe}/\text{H}] \rangle = -0.61 \pm 0.13$ between $80^{\circ} < \Lambda_{\odot} < 100^{\circ}$ (from 6 M giants), and $\langle [\text{Fe}/\text{H}] \rangle = -0.83 \pm 0.11$ (mean of 4 stars) for debris even further along the trailing tail. The existence of a metallicity gradient among Sgr stream M giants along both

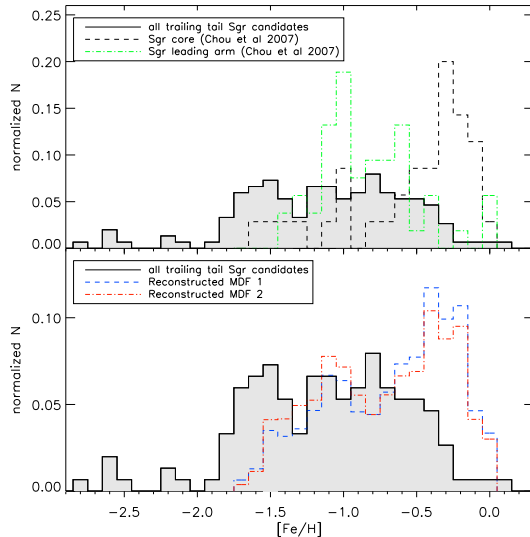


Figure 23. The normalized MDF from all 147 Sgr candidates in SAs 71, 94, 93, and 117 with spectra having $S/N > 20$ is shown as a solid black histogram with grey fill. For comparison, in the upper panel we show the MDFs from Chou et al. (2007) of the Sgr core (black dashed line) and Sgr leading arm M-giants (green dot-dashed line). In the lower panel the red (dot-dashed) and blue (dashed) histograms show the approximate Sgr MDF from several Gyr ago reconstructed by Chou et al. from linear combinations of the core and leading arm samples. The first of these was created by interpolating the MDFs at different orbital longitudes, and MDF 2 was created by assigning observed MDFs to particles in the Law et al. (2005) Sgr model by the times they became unbound.

the trailing and leading tails was confirmed by Keller et al. (2010), who combined their additional measurements of 5 stars at $\Lambda_{\odot} = 66^{\circ}$ ($\langle [\text{Fe}/\text{H}] \rangle \sim -0.5$) and 6 stars at $\Lambda_{\odot} = 132^{\circ}$ ($\langle [\text{Fe}/\text{H}] \rangle \sim -0.7$) with the Chou et al. and Monaco et al. results to confirm the gradient in $[\text{Fe}/\text{H}]$ among Sgr stream M-giants. However, all of these M-giant studies suffer an inherent bias toward metal-rich stellar populations, and are likely not showing the true MDF of the Sgr system.

Blue horizontal branch stars (BHBs) are another easily-identified and rather unambiguous tracer of halo substructure that has been used to probe the Sgr stream. However, BHB stars arise only in old, metal-poor populations, and are thus not ideal tracers of the global MDF of a system consisting of multiple stellar populations. Yanny et al. (2009b) performed an extensive study of the Sgr tails using SDSS and SEGUE spectroscopy of BHB stars in both the northern and southern Galactic caps. BHB stars in the portions of both the leading ($200^{\circ} < \Lambda_{\odot} < 300^{\circ}$) and trailing ($70^{\circ} < \Lambda_{\odot} < 110^{\circ}$) tails in this study have MDFs peaking at $\langle [\text{Fe}/\text{H}] \rangle \sim -1.7$, with significant numbers of stars as low as $[\text{Fe}/\text{H}] \sim -2.5$. Although this result turns up metal-poor populations not seen in M-giants, it is difficult to make conclusions about the overall MDF of the Sgr stream or progenitor based on biased metallicity tracers such as BHB stars and M-giants.

Fortunately, because the present analysis makes use of MSTO stars, it is far less susceptible to metallicity biases and can provide new insights into the MDF (particularly at the intermediate to metal-poor end) of the stream (and therefore the progenitor) MDF. Of course, our spectra have $\sim 10\times$ worse resolution than the various echelle resolution studies, but our sample of Sgr stream stars is significantly larger, including 147 with good enough S/N (> 20) for $[\text{Fe}/\text{H}]$ measurements to the approximately $\lesssim 0.3$ dex level. As shown in Figure 21 and 22, the mean $[\text{Fe}/\text{H}]$ for that portion of the stream probed

by our SA data is about -1.1 , but with a significant tail to both solar metallicity as well as very metal poor (< -2.0) stars. Indeed, our sample includes some rather metal-poor stars associated with the Sgr system, with stars as metal-poor as the -2.5 dex BHBs seen by Yanny et al. (2009b).

Figure 23 shows the MDF derived from our data in the $88^{\circ} < \Lambda_{\odot} < 128^{\circ}$ portion of the Sgr trailing tail. The MDF we derive is significantly broader and extending to much more metal-poor stars than indicated by the biased, M-giant studies (shown in the upper panel of Figure 23 as a black dashed histogram for the Sgr core and green dot-dashed lines for the leading arm), encompassing both the M-giant and BHB results. A comparison of our MDF to the Chou et al. (2007) reconstruction of the Sgr M-giant MDF from several Gyr ago based on their core and leading-arm samples is given in the lower panel of Figure 23. Clearly our Sgr trailing-tail sample is lacking the metal-rich component seen in the present-day core, but shows a similar distribution to the metal-poor tail of the reconstructed MDF. Additional metal-poor stars are present in our sample that are not seen in the M-giant samples; these are likely drawn from similar populations to those in the Yanny et al. (2009b) study.

Obviously, as has been shown by Chou et al. and others, the total MDF of the entire Sgr system will include a higher contribution of metal-rich stars when the core is included, but we also expect more metal-poor stars from those parts of the tails with larger separation from the core than we explore. Thus, while we cannot yet accurately reconstruct the total MDF of the Sgr system, at least we now have a better feel of the *breadth* of the Sgr MDF from the data shown in Figures 21 and 23. Comparison of the latter MDF with those of other MW dSphs (summarized, e.g., in Kirby et al. 2011) shows Sgr to be more typical of other MW satellites. In particular, the Sgr MDF resembles even more that of the LMC (as has been previously suggested by, e.g., Monaco et al. 2003, Cole et al. 2005, and Monaco et al. 2005), which has been argued to be a chemical analog to the Sgr progenitor by Chou et al. (2010) and a morphological analog by Łokas et al. (2010).

5.3. “Alpha” Abundances

As shown in Section 5.1, we have identified metal-poor populations in (at least) four of the fields from our study, which explore a different segment of the stellar populations in the Sgr stream than previous M-giant studies. We have observed stars in these fields only at low resolution, and thus cannot do detailed element-by-element chemical analysis such as that enabled by high-resolution spectroscopy. However, we can use the low-resolution Lick indices to explore relative α -abundances for the stars in our study. Specifically, we explore the relative Mg abundances using the Lick Mg b index centered at 5160-5190 Å. Calibrating the Mg b index to an actual $[\text{Mg}/\text{Fe}]$ abundance is difficult, because the strength of Mg lines is highly sensitive to surface gravity, with some additional sensitivity to effective temperature and $[\text{Fe}/\text{H}]$. Disentangling these effects is difficult with low-resolution spectra, but we can still explore a subset of the stars in our samples in a way that is relatively free of the effects of surface gravity and temperature of individual stars. To do so, we select only blue ($0.2 < g-r < 0.7$, or $B-V < 0.9$) stars, which should be mostly main-sequence dwarfs (thus, with similar surface gravity), since no giants are found at such blue colors. Furthermore, the temperature sensitivity of the Mg line strength, which is already much smaller than the log g sensi-

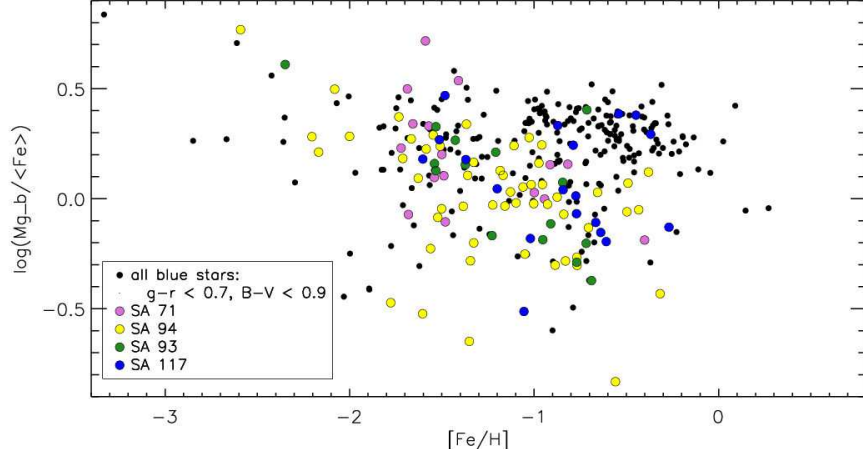


Figure 24. Relative values of Lick index ratio $\log(\text{Mg b}/\langle\text{Fe}\rangle)$, where the indices are as described in the text and Carlin et al. 2011 (*in prep.*), for all blue stars ($0.2 < g-r < 0.7$ for SAs 94 and 93, and $B-V < 0.9$ for SAs 71 and 117) having spectra with $S/N > 30$ in the four SA fields with securely identified Sgr debris. When comparing only predominantly dwarf stars of similar, blue photometric colors, the $\log(\text{Mg b}/\langle\text{Fe}\rangle)$ ratio can be thought of as a proxy for $[\text{Mg}/\text{Fe}]$, because variations in $[\text{Mg}/\text{Fe}]$ with $\log g$ and color (i.e., temperature) are then minimized. Colored points represent all stars within the initial Sgr candidate RV selections, with color codes as in the legend. Black dots are all other stars outside the Sgr velocity range. For $[\text{Fe}/\text{H}] \gtrsim -1.5$, Sgr candidates (colored points) typically occupy a region of lower Mg abundance at a given $[\text{Fe}/\text{H}]$ than the black dots that are likely Galactic foreground stars. This behavior is typical for stars from most Galactic dSphs (relative to Galactic disk populations). At lower metallicities, the distributions converge.

tivity, is mitigated by concentrating on a limited color range. In Figure 24 we show a “pseudo- $[\text{Mg}/\text{Fe}]$ ” ratio, given as the logarithm of the ratio of the Lick Mg b index to the mean of all eight Lick Fe indices (after transforming them to a common scale), for all of the blue stars in SAs 71, 94, 93, and 117 for which we have high enough signal-to-noise (> 30) to precisely measure indices and $[\text{Fe}/\text{H}]$. Black points in this diagram are all stars with non-Sgr radial velocities, while our samples of all stars with Sgr-like RVs in each field are shown as colored points. It is readily apparent that the black (MW) points mostly occupy a different region of the diagram than the colored (Sgr) dots, which suggests an intrinsic chemical difference between the populations (though some overlap is expected, especially at low metallicities, where many MW halo stars likely resemble dSphs in their abundance patterns). Indeed, the behavior seen in Figure 24 is exactly that seen for many MW dSphs – for more metal-rich dSph stars, the Mg (or α) abundance is lower (on average) at a given $[\text{Fe}/\text{H}]$ than in the Galactic populations, with the two populations converging at lower metallicities (i.e., at the “knee” in the dSph’s distribution). Among the more metal-rich (and younger) M-giant populations of the Sgr stream, there is some indication that the knee in $[\alpha/\text{Fe}]$ occurs at $-1.2 \lesssim [\text{Fe}/\text{H}] \lesssim -1.0$ (Chou et al. 2010; Monaco et al. 2007), but this is difficult to assess because of the lack of M-giants at lower metallicity. Thus the apparent convergence of Sgr trailing tail $[\text{Mg}/\text{Fe}]$ with the plateau seen in Galactic stars at $[\text{Fe}/\text{H}] \lesssim -1.5$ may be an extension of the same behavior seen in the M-giant studies. Alternatively, since we’ve already shown that the mean $[\text{Fe}/\text{H}]$ along the trailing tail differs between the M-giant sample of Monaco et al. (2007), who find $[\text{Fe}/\text{H}] \sim -0.6$, and our result of $[\text{Fe}/\text{H}] \sim -1.2$ (which is also consistent with the findings of Sesar et al. 2010), our study may be sampling a distinctly older, more metal-poor population of Sgr debris than the M-giant tracers. Further characterization of the α -element behavior along the Sgr trailing tail would benefit from either a calibration of our $\text{Mg b}/\langle\text{Fe}\rangle$ index onto $[\text{Mg}/\text{Fe}]$ abundance or the identification of bona fide stream giant stars that are bright enough for echelle-resolution spectroscopic follow-up.

6. SUMMARY

We have presented the first large-scale study of the 3-D kinematics of the Sagittarius trailing tidal stream, with data spanning $\sim 60^\circ$ along the trailing tail. The data include deep, precise proper motions derived from photographic plates with a ~ 90 -year baseline, and radial velocities from more than 1500 low-resolution stellar spectra, of which > 150 have been identified as Sgr debris stars. Mean absolute proper motions of these Sgr stars in four of the six $40' \times 40'$ fields from our survey have been derived with ~ 0.25 – 0.7 mas yr^{-1} per field precision in each dimension (depending on the quality and depth of plate material and the number of spectra obtained in each field). Mean three-dimensional kinematics in each of these four fields have been shown to agree with the predicted V_{GSR} and μ_b from the Sagittarius disruption models of LM10. However, there is a systematic disagreement in the $\mu_l \cos(b)$ proper motions (with the exception of the somewhat problematical SA 71 field), which we use to assess refinements to the mass scale of the Milky Way (particularly its disk and bulge components).

While proper motions along the portion of the trailing tail in this study provide constraints on Sgr tidal disruption models, the fortuitous orientation of the Sgr plane also allows us to use the measured proper motions to derive the circular velocity at the Solar circle (or “Local Standard of Rest”), Θ_{LSR} . Our first-order approximation using only the $\mu_l \cos(b)$ proper motions as constraints yields $\Theta_{\text{LSR}} = 264 \pm 23 \text{ km s}^{-1}$. From our measured 3-D kinematics, we find this fundamental Milky Way parameter to be $\Theta_{\text{LSR}} = 232 \pm 14 \text{ km s}^{-1}$, or $\sim 1\sigma$ higher than the IAU standard value of 220 km s^{-1} . When we remove SA 71, a field in which it is more difficult to unambiguously identify Sgr debris, from the sample we find $\Theta_{\text{LSR}} = 244 \pm 17 \text{ km s}^{-1}$. We suggest that the true value of Θ_{LSR} lies somewhere between 232 – 264 km s^{-1} , while noting that all three of these estimates are consistent with each other within their 1σ uncertainties.

Our general result that the circular velocity at the Solar radius is higher than the IAU standard of 220 km s^{-1} agrees with

the recent derivation of $\Theta_{\text{LSR}} = 254 \pm 16 \text{ km s}^{-1}$ by Reid et al. (2009) using trigonometric parallaxes of star forming regions in the outer disk. The same maser data from the Reid et al. study were reanalyzed by Bovy et al. (2009), and yield a result of $246 \pm 30 \text{ km s}^{-1}$ ($244 \pm 13 \text{ km s}^{-1}$ if priors on the proper motion of Sgr A* are included, and $236 \pm 11 \text{ km s}^{-1}$ if the additional contribution of orbital fitting to the GD-1 stellar stream is included). Again, our independent result is consistent with these studies, and inconsistent with the IAU accepted value of 220 km s^{-1} for this fundamental constant at the $1\text{-}\sigma$ level. Identification of additional Sgr candidates could increase the accuracy of our determination of Θ_{LSR} , as could the addition of another epoch of accurate data to the proper motion measurements.

We note that while Reid et al. (2009) argued that their measurement of 254 km s^{-1} would imply an upward revision of the total Milky Way mass by a factor of ~ 2 (to a mass similar to that of M31), we have shown that this is not required to produce Θ_{LSR} even higher than that of Reid et al. Scaling the Milky Way dark matter halo up in mass to a level that yields $\Theta_{\text{LSR}} = 264 \text{ km s}^{-1}$ while simultaneously reproducing known leading arm debris requires the Sgr core to have a high ($\sim 400 \text{ km s}^{-1}$) space velocity, resulting in RVs in the tidal streams that are discrepant by $\sim 75 \text{ km s}^{-1}$ from measured values. Instead, we show that because $> 80\%$ of the centripetal force at the location of the Sun is contributed by mass in the Galactic disk and bulge, an increase of $\sim 50\%$ in the mass of the disk+bulge accounts for the additional acceleration needed to produce 264 km s^{-1} rotation at the solar circle, while contributing only a small ($\sim 7\%$) increase to the total virial mass of the Milky Way. With the additional constraint on the disk+bulge mass provided by our measurement of Θ_{LSR} , we have found a satisfactory model of Sgr disruption that matches all of the constraints used in fitting the LM10 model, while additionally predicting a proper motion for the Sgr dwarf that is in much better agreement with observations than the LM10 model.

Stellar metallicities have been derived from the low-resolution spectra of Sgr candidates, and the mean metallicity of Sgr tidal debris derived in each field. We find that a constant $[\text{Fe}/\text{H}] = -1.15$ is consistent with the observations of all four fields for which Sgr members were reliably identified. However, a linear fit to these four data points suggests that a gradient of $(1.4 \times 10^{-3}) \text{ dex degree}^{-1}$ is also reasonable (though this value is consistent with zero slope within the uncertainty), in line with previous findings (e.g., Chou et al. 2007; Keller et al. 2010) of a metallicity gradient among M-giants along both the leading and trailing tidal tails. The scatter of $[\text{Fe}/\text{H}]$ in each of the survey fields is $\gtrsim 0.5 \text{ dex}$, which is typical of the stellar populations seen in the core of the Sgr dSph (e.g., Smecker-Hane & McWilliam 2002; Zaggia et al. 2004; Siegel et al. 2007; Monaco et al. 2005). We show the metallicity distribution function for the trailing tail that is free from the biases inherent in previous studies of the Sgr MDF. We find that the MDF of trailing debris is similar to MDFs of typical classical Milky Way dwarf spheroidals. A “pseudo- $[\text{Mg}/\text{Fe}]$ ” was measured based on the ratio of Lick Mg b and $\langle \text{Fe} \rangle$ indices; the behavior of $\log (\text{Mg b}/\langle \text{Fe} \rangle)$ with $[\text{Fe}/\text{H}]$ for Sgr main-sequence candidates is markedly different from Galactic stars of similar photometric colors (identified by radial velocity) from among the same datasets. Furthermore, the trend is similar to that typically seen for dSphs, in that $[\text{Mg}/\text{Fe}]$ is deficient at a given $[\text{Fe}/\text{H}]$ for Sgr stars relative to

the Milky Way field populations, and converges to a “knee” in Figure 24 at lower ($[\text{Fe}/\text{H}] \sim -1.5$) metallicity. This is a lower $[\text{Fe}/\text{H}]$ than previously reported for Sgr M giants, and may reflect a bias intrinsic to those earlier M-giant studies. High-resolution spectroscopic follow-up will be necessary to confirm this trend among the old, metal-poor populations of recently-stripped Sgr debris.

We appreciate the useful comments provided by the anonymous referee. We thank Mei-Yin Chou for kindly sharing the Sgr MDF data used in Figure 23, and Heidi Newberg for many useful discussions. JLC acknowledges support from National Science Foundation grant AST-0937523, and observing travel support from the NOAO thesis student program for proposal ID 2008B-0448. JLC and SRM acknowledge partial funding of this work from NSF grant AST-0807945 and NASA/JPL contract 1228235. DIC and TG acknowledge NSF grant AST-0406884. DRL acknowledges support provided by NASA through Hubble Fellowship grant # HF-51244.01 awarded by the Space Telescope Science Institute, which is operated by the Association of Universities for Research in Astronomy, Inc., for NASA, under contract NAS 5-26555.

SRM is grateful to Allan Sandage for alerting him to the existence of the Mt. Wilson Selected Areas plates, for suggesting their use as a first epoch to expand our proper motion work in Kapteyn Selected Areas, and for his contribution of KPNO plates to our survey.

Facilities: WIYN (Hydra), MMT (Hectospec), Sloan, Swope, MtW:1.5m, Du Pont, Mayall

Funding for the SDSS and SDSS-II has been provided by the Alfred P. Sloan Foundation, the Participating Institutions, the National Science Foundation, the U.S. Department of Energy, the National Aeronautics and Space Administration, the Japanese Monbukagakusho, the Max Planck Society, and the Higher Education Funding Council for England. The SDSS Web Site is <http://www.sdss.org/>.

The SDSS is managed by the Astrophysical Research Consortium for the Participating Institutions. The Participating Institutions are the American Museum of Natural History, Astrophysical Institute Potsdam, University of Basel, University of Cambridge, Case Western Reserve University, University of Chicago, Drexel University, Fermilab, the Institute for Advanced Study, the Japan Participation Group, Johns Hopkins University, the Joint Institute for Nuclear Astrophysics, the Kavli Institute for Particle Astrophysics and Cosmology, the Korean Scientist Group, the Chinese Academy of Sciences (LAMOST), Los Alamos National Laboratory, the Max-Planck-Institute for Astronomy (MPIA), the Max-Planck-Institute for Astrophysics (MPA), New Mexico State University, Ohio State University, University of Pittsburgh, University of Portsmouth, Princeton University, the United States Naval Observatory, and the University of Washington.

REFERENCES

- Abadi, M. G., Navarro, J. F., Steinmetz, M., & Eke, V. R. 2003, *ApJ*, 591, 499
- Abazajian, K. N., Adelman-McCarthy, J. K., Agüeros, M. A., et al. 2009, *ApJS*, 182, 543
- Alard, C. 2001, *A&A*, 377, 389
- Andrae, R. 2010, *arXiv:1009.2755*
- Bedin, L. R., Piotto, G., King, I. R., & Anderson, J. 2003, *AJ*, 126, 247
- Bellazzini, M., Ferraro, F. R., & Ibata, R. 2003, *AJ*, 125, 188
- Bellazzini, M., Newberg, H. J., Correnti, M., Ferraro, F. R., & Monaco, L. 2006, *A&A*, 457, L21
- Belokurov, V., Zucker, D. B., Evans, N. W., et al. 2006, *ApJ*, 642, L137
- Belokurov, V., Evans, N. W., Irwin, M. J., et al. 2007, *ApJ*, 658, 337

- Bovy, J., Hogg, D. W., & Rix, H. 2009, *ApJ*, 704, 1704
- Bullock, J. S., & Johnston, K. V. 2005, *ApJ*, 635, 931
- Carlin, J. L., Casetti-Dinescu, D. I., Grillmair, C. J., Majewski, S. R., & Girard, T. M. 2010, *ApJ*, 725, 2290
- Carraro, G., Zinn, R., & Moni Bidin, C. 2007, *A&A*, 466, 181
- Casetti-Dinescu, D. I., Carlin, J. L., Girard, T. M., et al. 2008, *AJ*, 135, 2013
- Casetti-Dinescu, D. I., Girard, T. M., Majewski, S. R., et al. 2009, *ApJ*, 701, L29
- Casetti-Dinescu, D. I., Majewski, S. R., Girard, T. M., et al. 2006, *AJ*, 132, 2082
- Chou, M., Cunha, K., Majewski, S. R., et al. 2010, *ApJ*, 708, 1290
- Chou, M., Majewski, S. R., Cunha, K., et al. 2007, *ApJ*, 670, 346
- Cole, A. A., Tolstoy, E., Gallagher, III, J. S., & Smecker-Hane, T. A. 2005, *AJ*, 129, 1465
- Correnti, M., Bellazzini, M., Ibata, R. A., Ferraro, F. R., & Varghese, A. 2010, *ApJ*, 721, 329
- Dehnen, W., & Binney, J. J. 1998, *MNRAS*, 298, 387
- Dinescu, D. I., Girard, T. M., van Altena, W. F., & López, C. E. 2005, *ApJ*, 618, L25
- Dinescu, D. I., Majewski, S. R., Girard, T. M., & Cudworth, K. M. 2000, *AJ*, 120, 1892
- Dinescu, D. I., Majewski, S. R., Girard, T. M., et al. 2002, *ApJ*, 575, L67
- Dohm-Palmer, R. C., Helmi, A., Morrison, H. L., et al. 2001, *ApJ*, 555, L37
- Fabricant, D., Fata, R., Roll, J., et al. 2005, *PASP*, 117, 1411
- Feast, M., & Whitelock, P. 1997, *MNRAS*, 291, 683
- Fellhauer, M., Belokurov, V., Evans, N. W., et al. 2006, *ApJ*, 651, 167
- Font, A. S., Johnston, K. V., Bullock, J. S., & Robertson, B. E. 2006, *ApJ*, 638, 585
- Friel, E. D. 1987, *AJ*, 93, 1388
- Frinchaboy, P. M., Muñoz, R. R., Phelps, R. L., Majewski, S. R., & Kunkel, W. E. 2006, *AJ*, 131, 922
- Geisler, D., Smith, V. V., Wallerstein, G., Gonzalez, G., & Charbonnel, C. 2005, *AJ*, 129, 1428
- Ghez, A. M., Salim, S., Weinberg, N. N., et al. 2008, *ApJ*, 689, 1044
- Girardi, L., Grebel, E. K., Odenkirchen, M., & Chiosi, C. 2004, *A&A*, 422, 205
- Grillmair, C. J. 2006a, *ApJ*, 645, L37
- . 2006b, *ApJ*, 651, L29
- . 2009, *ApJ*, 693, 1118
- Grillmair, C. J., & Dionatos, O. 2006, *ApJ*, 643, L17
- Hargreaves, J. C., Gilmore, G., Irwin, M. J., & Carter, D. 1994, *MNRAS*, 269, 957
- Helmi, A. 2004, *ApJ*, 610, L97
- Helmi, A., & White, S. D. M. 2001, *MNRAS*, 323, 529
- Ibata, R., Lewis, G. F., Irwin, M., Totten, E., & Quinn, T. 2001, *ApJ*, 551, 294
- Ibata, R. A., Gilmore, G., & Irwin, M. J. 1994, *Nature*, 370, 194
- Ibata, R. A., Irwin, M. J., Lewis, G. F., Ferguson, A. M. N., & Tanvir, N. 2003, *MNRAS*, 340, L21
- Johnston, K. V., Law, D. R., & Majewski, S. R. 2005, *ApJ*, 619, 800
- Johnston, K. V., Spergel, D. N., & Hernquist, L. 1995, *ApJ*, 451, 598
- Johnston, K. V., Zhao, H., Spergel, D. N., & Hernquist, L. 1999, *ApJ*, 512, L109
- Jones, L. A. 1998, PhD thesis, The University of North Carolina at Chapel Hill
- Kalirai, J. S., Richer, H. B., Hansen, B. M., et al. 2004, *ApJ*, 601, 277
- Kapteyn, J. C. 1906, Plan of selected areas (Groningen, Hoitsema brothers, 1906.)
- Keller, S. C., Yong, D., & Da Costa, G. S. 2010, *ApJ*, 720, 940
- Kerr, F. J., & Lynden-Bell, D. 1986, *MNRAS*, 221, 1023
- Kirby, E. N., Lanfranchi, G. A., Simon, J. D., Cohen, J. G., & Guhathakurta, P. 2011, *ApJ*, 727, 78
- Kleyna, J., Wilkinson, M. I., Evans, N. W., Gilmore, G., & Frayn, C. 2002, *MNRAS*, 330, 792
- Koposov, S. E., Rix, H., & Hogg, D. W. 2010, *ApJ*, 712, 260
- Kuijken, K., & Tremaine, S. 1994, *ApJ*, 421, 178
- Law, D. R., Johnston, K. V., & Majewski, S. R. 2005, *ApJ*, 619, 807
- Law, D. R., & Majewski, S. R. 2010a, *ApJ*, 714, 229 (LM10)
- . 2010b, *ApJ*, 718, 1128
- Law, D. R., Majewski, S. R., & Johnston, K. V. 2009, *ApJ*, 703, L67
- Łokas, E. L., Kazantzidis, S., Majewski, S. R., et al. 2010, *ApJ*, 725, 1516
- Majewski, S. R. 1992, *ApJS*, 78, 87
- . 1993, *ARA&A*, 31, 575
- Majewski, S. R. 1999, in *Astronomical Society of the Pacific Conference Series*, Vol. 165, The Third Stromlo Symposium: The Galactic Halo, ed. B. K. Gibson, R. S. Axelrod, & M. E. Putman, 76–+
- Majewski, S. R., Law, D. R., Polak, A. A., & Patterson, R. J. 2006, *ApJ*, 637, L25 (MLPP)
- Majewski, S. R., Munn, J. A., & Hawley, S. L. 1996, *ApJ*, 459, L73+
- Majewski, S. R., Skrutskie, M. F., Weinberg, M. D., & Ostheimer, J. C. 2003, *ApJ*, 599, 1082
- Majewski, S. R., Kunkel, W. E., Law, D. R., et al. 2004, *AJ*, 128, 245
- Martínez-Delgado, D., Gómez-Flechoso, M. Á., Aparicio, A., & Carrera, R. 2004, *ApJ*, 601, 242
- Mihalas, D., & Binney, J. 1981, *Galactic astronomy: Structure and kinematics /2nd edition/* (W. H. Freeman and Co.)
- Mink, D. J., Wyatt, W. F., Caldwell, N., Conroy, M. A., Furesz, G., & Tokarz, S. P. 2007, in *Astronomical Society of the Pacific Conference Series*, Vol. 376, *Astronomical Data Analysis Software and Systems XVI*, ed. R. A. Shaw, F. Hill, & D. J. Bell, 249–+
- Miyamoto, M., & Nagai, R. 1975, *PASJ*, 27, 533
- Monaco, L., Bellazzini, M., Bonifacio, P., et al. 2007, *A&A*, 464, 201
- Monaco, L., Bellazzini, M., Bonifacio, P., et al. 2005, *A&A*, 441, 141
- Monaco, L., Bellazzini, M., Ferraro, F. R., & Pancino, E. 2003, *ApJ*, 597, L25
- Muñoz, R. R., Carlin, J. L., Frinchaboy, P. M., et al. 2006a, *ApJ*, 650, L51
- Muñoz, R. R., Majewski, S. R., & Johnston, K. V. 2008, *ApJ*, 679, 346
- Muñoz, R. R., Majewski, S. R., Zaggia, S., et al. 2006b, *ApJ*, 649, 201
- Munn, J. A., Monet, D. G., Levine, S. E., et al. 2004, *AJ*, 127, 3034
- . 2008, *AJ*, 136, 895
- Newberg, H. J., Yanny, B., Rockosi, C., et al. 2002, *ApJ*, 569, 245
- Olling, R. P., & Merrifield, M. R. 1998, *MNRAS*, 297, 943
- Peñarrubia, J., Belokurov, V., Evans, N. W., et al. 2010, *MNRAS*, 408, L26
- Pryor, C., & Meylan, G. 1993, in *Astronomical Society of the Pacific Conference Series*, Vol. 50, *Structure and Dynamics of Globular Clusters*, ed. S. G. Djorgovski & G. Meylan, 357
- Pryor, C., Piatek, S., & Olszewski, E. W. 2010, *AJ*, 139, 839
- Reid, M. J., & Brunthaler, A. 2004, *ApJ*, 616, 872
- Reid, M. J., Menten, K. M., Zheng, X. W., et al. 2009, *ApJ*, 700, 137
- Robin, A. C., Reylé, C., Derrière, S., & Picaud, S. 2003, *A&A*, 409, 523
- Sbordone, L., Bonifacio, P., Buonanno, R., et al. 2007, *A&A*, 465, 815
- Schiavon, R. P. 2007, *ApJS*, 171, 146
- Schlegel, D. J., Finkbeiner, D. P., & Davis, M. 1998, *ApJ*, 500, 525
- Searles, F. H., Kapteyn, J. C., van Rhijn, P. J., Joyner, M. C., & Richmond, M. L. 1930, Mount Wilson catalogue of photographic magnitudes in selected areas 1-139 (Carnegie institution of Washington)
- Searle, L., & Zinn, R. 1978, *ApJ*, 225, 357
- Sesar, B., Ivezić, Ž., Grammer, S. H., et al. 2010, *ApJ*, 708, 717
- Shetrone, M., Venn, K. A., Tolstoy, E., et al. 2003, *AJ*, 125, 684
- Shetrone, M. D., Côté, P., & Sargent, W. L. W. 2001, *ApJ*, 548, 592
- Siegel, M. H., Dotter, A., Majewski, S. R., et al. 2007, *ApJ*, 667, L57
- Siegel, M. H., et al. 2011, *ApJ*, accepted (arXiv:1108.6276)
- Smecker-Hane, T. A., & McWilliam, A. 2002, *ArXiv:0205411*
- Sofue, Y., Honma, M., & Omodaka, T. 2009, *PASJ*, 61, 227
- Sohn, S. T., Majewski, S. R., Muñoz, R. R., et al. 2007, *ApJ*, 663, 960
- Tolstoy, E., Hill, V., & Tosi, M. 2009, *ARA&A*, 47, 371
- Tolstoy, E., Venn, K. A., Shetrone, M., et al. 2003, *AJ*, 125, 707
- Tonry, J., & Davis, M. 1979, *AJ*, 84, 1511
- van Leeuwen, F. 2007, *A&A*, 474, 653
- Venn, K. A., Irwin, M., Shetrone, M. D., et al. 2004, *AJ*, 128, 1177
- Vogt, S. S., Mateo, M., Olszewski, E. W., & Keane, M. J. 1995, *AJ*, 109, 151
- Worthey, G., Faber, S. M., Gonzalez, J. J., & Burstein, D. 1994, *ApJS*, 94, 687
- Yanny, B., Newberg, H. J., Grebel, E. K., et al. 2003, *ApJ*, 588, 824
- Yanny, B., Rockosi, C., Newberg, H. J., et al. 2009a, *AJ*, 137, 4377
- Yanny, B., Newberg, H. J., Johnson, J. A., et al. 2009b, *ApJ*, 700, 1282
- Yuan, F., Zhu, Z., & Kong, D. 2008, *Chinese J. Astron. Astrophys.*, 8, 714
- Zaggia, S., Bonifacio, P., Bellazzini, M., et al. 2004, *Memorie della Società Astronomica Italiana Supplementi*, 5, 291